

LARGE AREA MULTIPixel PHOTON COUNTERS ON THE SEARCH FOR EXOTIC HYBRID MESONS AT GLUEX

A Thesis
Submitted to the Faculty of Graduate Studies and Research
In Partial Fulfillment of the Requirements
for the Degree of
Master of Science
In
Physics
University of Regina

by
Mehrnoosh Tahani
Regina, Saskatchewan
July, 2012

Copyright 2012: M. Tahani

Abstract

The GlueX project aims to elucidate the confinement property of quantum chromodynamics. Silicon PhotoMultipliers (SiPMs) will be the readout for the GlueX Barrel Calorimeter (BCAL), a key subsystem of the detector designed for the GlueX project. The important and most desired characteristic of SiPMs is their immunity to magnetic fields, since the BCAL is placed immediately in a 2.2 T solenoid. Other advantages compared to conventional PMTs is that they operate using low bias voltage ($< 100 V$), have higher photon detection efficiency, lower cost, and are more compact and robust. SiPMs offer much promise to revolutionize light detection in particle, but also medical and space physics, among other.

Hamamatsu, a Japanese photonics company, will manufacture the SiPMs for the BCAL. These photosensors are arrays of $16 - 3 \times 3 \text{ mm}^2$ SiPMs. In this thesis, discusses the test carried out for one 2010 Hamamatsu unit and ten 2011 (years of manufacture) first article Hamamatsu SiPM units. The tests are the first fiber-based tests for the SiPMs. The two major tests are the photon detection efficiency (PDE) and the gain uniformity of their cells and sub-cells. Depending on the method of measurement, the extracted PDE fell in the range of 15-30%, while the cells exhibited gain uniformity mostly within 10%. The result of this thesis will be directly used by the GlueX collaboration towards quality control of the 4000 units ordered for the BCAL.

Acknowledgments

I would like to thank my co-supervisors Dr. George. J. Lolos, and Dr. Z. Papandreou, for their advice, guidance, and patience. I appreciate the financial support I received through their NSERC grant.

I appreciate the great contribution to this research work by Mr. D. Kolybaba, Mr. K. Wolbaum, and Mr. D. Gervais, on the construction parts of the project, as well as their technical knowledge and advice. Dr. A. Semenov's suggestions in experimental designs in different aspects of this project were a great resource.

I would like to thank the GlueX collaboration, particularly Dr. E. Smith, and Mr. F. Barbosa for their providing of details on SiPM experiments. I am grateful for the financial support in the form of Graduate Studies Scholarship and Graduate Teaching Scholarship received from the Faculty of Graduate Studies and Research.

My great appreciation goes to Dr. N. Mobed and Dr. N. Ashton for giving me the opportunity to join the GlueX group, and for their support.

I would like to thank my family for their precious encouragement and support. In addition to this, I acknowledge my friends and fellow students for their understanding and encouragement.

Dedication

Dedicated to the loving memory of my father, Davoud, and to my loving mother and brothers, Homa, Soroush, Farshad, and Kianoosh.

Contents

List of abbreviations	xi
1 Introduction	1
2 Quantum Chromodynamics	3
2.1 The Fundamental Interactions within the SM	3
2.2 The Basics of Quark Model and QCD	4
2.3 Confinement	6
2.4 Quantum Numbers	6
2.5 Exotic Mesons	8
2.6 Meson Spectroscopy	9
3 The GlueX Detector	11
3.1 Introduction	11
3.2 BCAL	14
3.2.1 Scintillating Fibers	15
3.2.2 BCAL Readout	17
4 Silicon PhotoMultiplier Basic Function	21
4.1 Introduction	21

4.2	Avalanche PhotoDiodes	22
4.2.1	APD Gain and Quantum Efficiency	24
4.3	Silicon Photomultipliers	25
4.4	Photon Detection Efficiency	26
4.4.1	Fill Factor	27
4.5	SiPM Noise	27
4.5.1	Dark Current	28
4.5.2	Cross Talk	28
4.6	Recovery Time	29
4.7	Linearity	29
4.8	Dynamic Range	30
5	Gain Uniformity of the 2010 and the 2011 SiPM Units	31
5.1	Introduction	31
5.2	Gain Uniformity Set-up	32
5.3	Gain Uniformity Result	33
5.3.1	Forward Scan	34
5.3.2	Backward Scan	35
5.3.3	Random Scan	36
5.3.4	Cell Mapping	38
5.4	Consistency Checks	39
5.4.1	LED Investigation	39
5.4.2	Sub-Cell Geometry Study	40
5.5	First Article Units (2011 Pre-Production SiPM Units)	45
5.5.1	Visual Inspection	45
5.5.2	Gain Uniformity Tests for the 10, 2011 Article Units	46

5.5.3	Results of the Gain Uniformity Tests for the 10, 2011 Article Units	47
6	Photon Detection Efficiency Extraction	51
6.1	PDE Device Construction	51
6.2	PDE Measurements	57
6.2.1	Symmetry of the PDE Device	59
6.2.2	SiPM vs. PMT Using an External Trigger	61
6.2.3	Photodiode Current Scan Over the Laser Frequency	63
6.2.4	Frequency and Intensity Scan, Photodiode vs. PMT, Laser Triggered Externally	65
6.2.5	ADC Background	66
6.3	Intensity Scan, Photodiode vs. SiPM, Laser Triggered Internally . . .	68
6.4	PDE Extraction for the First Article Units	69
6.4.1	Incident Photon Determination	72
6.4.2	PDE Extraction Methods	74
6.4.3	Laser Intensity Scan	76
7	Conclusions	85
	Appendices	92
A	Plots for the Gain Uniformity and the PDE Measurements	92
A.1	The 2010 SiPM Unit	92
A.2	The 2011, 10 Article Units	94

List of Figures

1.1	The configuration for the 12 <i>GeV</i> upgrade of CEBA	2
2.1	The spin-0 mesons	5
3.1	GlueX detector at Hall D	13
3.2	Schematic view of the photon beam	13
3.3	Sketch of the Barrel Calorimeter readout	15
3.4	End view of a small section of a BCAL module	16
3.5	Graphic schematic of the critical angles in a double clad fiber	17
3.6	SiPM's position at the BCAL	18
3.7	A 3D rendering of figure 3.6, and a picture of a board containing all 40 SiPMs for one side of one module.	19
3.8	Design of a simple PMT	19
4.1	The breakdown voltage and the avalanche current for an APD	23
4.2	Basic structure of an APD	24
4.3	The structure for a simple APD and the electric field profile of the structure	25
4.4	The pulse of a SiPM unit, using the laser as the light source	26
4.5	Array of APDs	28

5.1	Schematic view of the SiPMs' cells and sub-cells	32
5.2	Gain uniformity test setup	34
5.3	Path of the X-Y scanner in the forward scan	35
5.4	Path of the X-Y scanner in the backward scan	35
5.5	Gain uniformity scans for the 2010 unit in a two dimensional representation	37
5.6	Path of the X-Y scanner for the cell mapping	38
5.7	Cell mapping scans for the 2010-pre-production unit carried out on different days	39
5.8	Illumination of sub-cells due to the distance between the SiPM and the fiber, in the absence of a collimator	41
5.9	A Schematic view of the SiPM's sub-cell families	42
5.10	Fired active areas for different families	44
5.11	Schematic view of the Hamamatsu model S10943-0258(X) SiPM array	46
5.12	Gain uniformity results for SiPM unit #75, 2D representation	48
5.13	Gain uniformity results for SiPM unit #75, deviation from average .	49
5.14	Gain uniformity scans for all the 10 article units excluding unit 75 . .	50
6.1	Fiber Holder and Light Guide (FHLG) apparatus for the PDE measurements	52
6.2	Details of the fiber holder for the PDE measurements	53
6.3	Light guide's dimensions in inches for the FHLG	54
6.4	Cylinder to hold the SiPM in the FHLG	55
6.5	Cylinder to hold the photodiode in the FHLG	55
6.6	Hamamatsu SiPM showing the inactive area at its centre, and pinout connections on the back.	56

6.7	The active area illuminated by the laser for the PDE measurement . .	57
6.8	The PDE electronic circuits when the UV LED is being used	59
6.9	The PDE electronic circuits when the laser is being used	59
6.10	A picture of the FHLG in the dark box	60
6.11	A picture of the oscilloscope, laser and the power supplies for the pre-amplifier and the bias voltages	60
6.12	A test on the symmetry of the FHLG	61
6.13	SiPM NPe values with an external trigger being used	62
6.14	PMT values with an external trigger being used	63
6.15	Laser intensity investigation by means of the SiPM	64
6.16	Laser intensity investigation with the Hamamatsu photodiode utilized	65
6.17	Photodiode and PMT response to the external frequency of the trigger for seven different intensity levels of the laser. (original in color) . . .	67
6.18	Observation for the dark current at different times	68
6.19	The SiPM's dark noise	69
6.20	The electronic noise in the PDE test set-up	70
6.21	ADC pedestal	71
6.22	First set of PDE measurements, photodiode current versus the pedestal- subtracted ADC value	72
6.23	First set of PDE measurements showing NPe versus the pedestal- subtracted ADC value	72
6.24	PDE extraction, using LED and intensity scan	78
6.25	PDE extraction, using LED and intensity scan	79
6.26	relative spectral intensity of a Kuraray SCSF-78MJ blue-green fiber .	80
6.27	S and QE of the Hamamatsu photodiode	81

6.28	Pulse shape of one of the SiPM units	82
6.29	Top panel: The number of photons and number of photoelectrons from all three methods are plotted on the left and right vertical axes. Bottom panel: The PDE extracted by all three methods. (original in color)	83
6.30	PDE values using the laser intensity scan	84
A.1	studying sub-cell families	93
A.2	studying sub-cell families	94
A.3	Gain uniformity test results for SiPMs #75 to 77	95
A.4	gain uniformity test results for SiPMs #77 to 79	96
A.5	gain uniformity test results for SiPMs #80 to 81	97
A.6	gain uniformity test results for SiPMs #81 to 85	98

List of Tables

2.1	The non-exotic $q\bar{q}$ mesons' quantum numbers	8
2.2	The exotic $q\bar{q}$ mesons' quantum numbers	8
2.3	Eight nonets of hybrid mesons	9
5.1	Sub-cell pulse heights for pulse 1	42
5.2	Sub-cell pulse heights for pulse 2	43
5.3	Pulse height averages	45
5.4	Visual Inspection of the 10, 2011-pre-production units	45
5.5	Bias Voltages for the first article units	47
6.1	Parameters of the double Moyal function, for the 10-cm and 30-cm fits. . .	74
6.2	PDE values for the 10, 2011 article units using the LED	75
6.3	PDE values for the three of the units by using the laser	76

List of abbreviations

ADC Analog to Digital Converter

AMPD Avalanche Microchannel PhotoDiode

APD Avalanche PhotoDiode

BCAL Barrel Calorimeter

CEBA Continuous Electron Beam Accelerator

FHLG Fiber Holder and Light Guide

G-APD Geiger-mode Avalanche PhotoDiode

JLab Jefferson Laboratory

LED Light Emitting Diode

Linac Linear Accelerator

MPPC Multi-Pixel Photon Counter

MRI Magnetic Resonance Imaging

MRS APD Avalanche PhotoDiodes with Metal-Resistance-Semiconductor structure

NPe Number of Photoelectrons

NPho Number of Photons

PDE Photon Detection Efficiency

PET Positron Emission Tomography

PMT PhotoMultiplier Tube

PWA Partial Wave Analysis

QCD Quantum Chromodynamics

QE Quantum Efficiency

QED Quantum Electrodynamics

RF Radio Frequency

SiPM Silicon PhotoMultiplier

SM Standard Model

SSPM Solid State PhotoMultiplier

TDC Time to Digital Converter

UV UltraViolet

Chapter 1

Introduction

The Thomas Jefferson National Accelerator Facility, commonly referred as Jefferson Lab (JLab), is an intermediate energy physics laboratory in Newport News, Virginia, United States. JLab contains four research areas referred to as Halls A, B, C, and D. One of the projects that will be carried out in Hall D is GlueX, which stands for Gluonic Excitations Experiment, and its main objective is to understand the nature of quark confinement.

The accelerator in JLab – Continuous Electron Beam Accelerator (CEBA)– uses a spin-polarized electron source. It also consists of an injector and two linear radio frequency (RF) accelerators, as shown in figure 1.1, which are the largest superconducting RF linear accelerators (linacs) in the world. The two linacs are connected together through arc sections. The electron beam is produced in the injector with an energy of 45 MeV , and it is injected into the accelerators every 0.667 ns [1]. The electron beam will go to the linacs and arc sections, several times. To reach an the energy of 6 GeV , the beam has to complete five turns, termed passes, in

the accelerator. JLab will upgrade the beam transport system from 6 to 12 GeV through extensive re-use and modification of existing hardware; and the addition of one recirculation arc [2]. In other words, for each linac side five cryomodules will be added, as shown in figure 1.1. Addition of the recirculation arc section allows the beam to go to its sixth pass through one of the linacs. Thus the energy of the electron beam going to Halls A, B, and C will be around 11 GeV . However, the electron beam going to Hall D will have the energy of 12.1 GeV , since Hall D is opposite to the other three Halls, as shown in figure 1.1.

In chapters 1 and 2 the basic physics concepts of the GlueX experiment will be presented. In chapter 3 a brief description of the GlueX detector is discussed, while a general overview on SiPMs is provided in chapter 4. The study of the SiPM gain uniformity and PDE is shown in chapters 5 and 6. Lastly, this thesis includes a brief conclusion and an appendix.

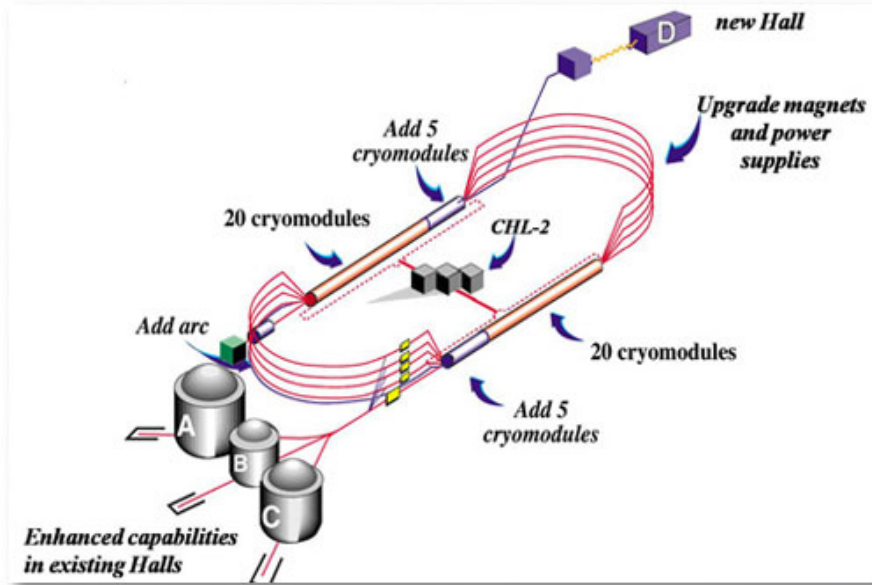


Figure 1.1: The configuration for the 12 GeV upgrade of CEBA at JLab showing the additional new Hall D for the GlueX experiment [3]. (original in color)

Chapter 2

Quantum Chromodynamics

2.1 The Fundamental Interactions within the SM

The four fundamental forces in the universe are gravity, weak force, strong force, and electromagnetic force. The Standard Model (SM), as the theory of particle physics, describes the three fundamental forces excluding gravity. According to the SM, the fundamental building blocks of matter, quarks and leptons, interact with each other exchanging bosons (force field particles), known as gauge bosons. The Electromagnetic force is described within the quantum field theory of electrodynamics (QED). The gauge bosons for the QED are photons, and the gauge bosons for the weak interactions are Z^0 , W^+ , and W^- . In the unified electroweak theory, the gauge bosons are the photon, Z^0 , W^+ , and W^- . The mediators for the strong force are known as gluons, which are described in quantum chromodynamics (QCD), as the quantum field theory of strong interaction. As the SM describes, these elementary particles, which interact via the strong force, are quarks and gluons. Thus, in terms of the strong force, quarks interact with each other exchanging gluons.

2.2 The Basics of Quark Model and QCD

According to the SM, as the electric charge is the source for electrodynamics, colour charges are the sources of the strong force. Conservation of electric charge results in the $U(1)$ symmetry, which represents electromagnetic interactions. The $SU(2)$ symmetry group describes weak interactions algebraically, which corresponds to conservation of a quantum number called “weak isospin”. The $SU_c(3)$ color symmetry group represents QCD. A quark can take on one of the values of red, green, or blue as a color charge, while an anti-quark can have one of the color charges of anti-red, anti-green, or anti-blue. Gluons are combinations of two colors.

The combination of the $U(1)$, $SU(2)$, and $SU(3)$ symmetry gauge groups is written as $SU(3) \times SU(2) \times U(1)$. The Unification of weak and electromagnetic interactions is described in $SU(2) \times U(1)$, known as electroweak interaction, which experimentally has been verified by the discovery of neutral weak currents in 1973 and by discoveries of the W^\pm and Z bosons in 1983.

As far as the strong interaction is concerned, so far, six quarks have been discovered, which are named up (u), down (d), strange (s), charm (c), top (t), and bottom (b). The first three are the lightest (u,d,s), and the three latter are the heaviest quarks (c,t,b). One of the relatively old models trying to describe quarks in terms of strong force is the “quark model”. The basic postulate of the quark model is that all hadrons are bound states of quarks [4]. The original quark model was based on the three lightest quarks. The three lightest quarks form a flavour $SU(3)$ ($SU(3)_f$) symmetry group. Combinations of quarks form the category of strongly interacting particles are known as hadrons.

Combinations of a quark and an anti-quark form mesons. As the $SU_f(3)$ symmetry group describes, a quark and an anti-quark form a nonet:

$$3 \otimes \bar{3} = 1 \oplus 8 \quad (2.1)$$

Where 3 represents the three flavour quarks, and $\bar{3}$ represents the three anti-quarks. $1 \oplus 8$ means that the result is a combination of eight objects (the octet) that transforms into itself under $SU_f(3)$ and a singlet. Figure 2.1 shows the spin-zero mesons, which form a nonet.

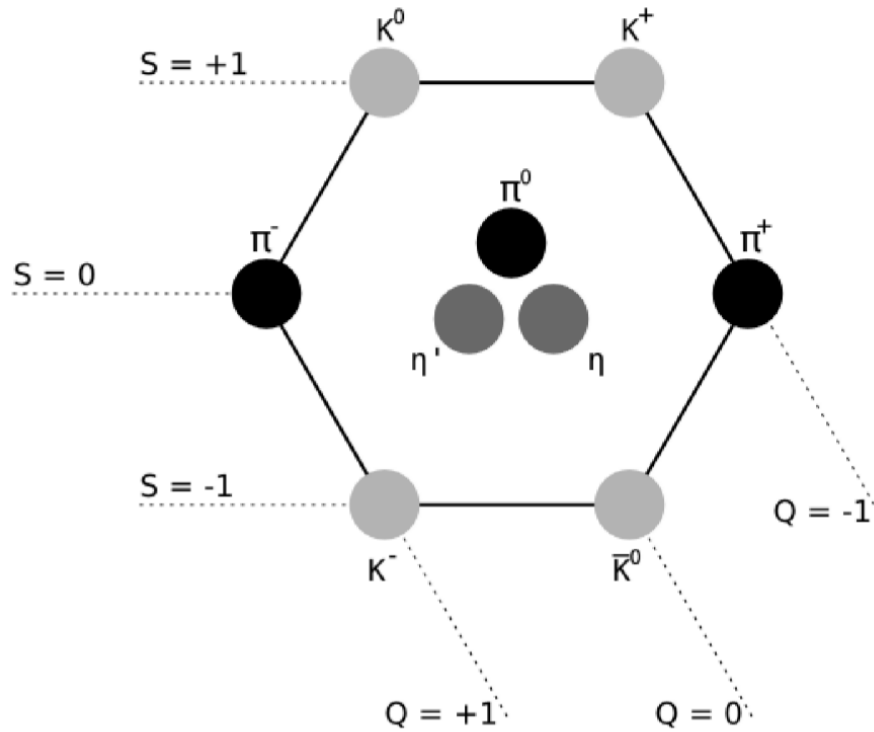


Figure 2.1: The spin-0 mesons.

2.3 Confinement

At short distances ($r < 10^{-13} \text{ cm}$), quarks and gluons interact very weakly, and strong interactions are described in the regime of asymptotic freedom, with the potential for one exchange gluon being:

$$V(r) \sim \frac{1}{r} \quad (2.2)$$

At distances of $r > 10^{-13} \text{ cm}$ quarks are confined [4]. The strong force between two quarks does not decrease with distance. This phenomenon is named confinement, which is an experimental fact that has been incorporated in QCD. In the early days of QCD, it was referred as “infrared slavery” [5]. To find the confinement potential some hints are provided through lattice gauge theory. Some physicists assume $V_{con}(r) \sim r$, others assume $V_{con}(r) \sim \ln(r)$, and others assume $V_{con}(r) \sim V_0$ [4]. For all the assumed potentials, infinite amount of energy is required to separate two quarks. Thus, if we choose $V_{con}(r) \sim r$, then:

$$V_{QCD}(r) = V_{gluon}(r) + V_{conf}(r) = -\frac{4}{3} \frac{\alpha_s}{r} + F_0 r \quad (2.3)$$

where r is the distance, α_s is a constant which is called the fine structure constant, and F_0 is a constant.

2.4 Quantum Numbers

As discussed, mesons are grouped in nonets, each characterized by unique quantum numbers (states of J^{PC}), which are the total angular momentum (J), parity (P), and

C-parity or charge conjugation (C). J can be found from the system's total angular momentum (\vec{L}) and its total spin (\vec{S}). Thus:

$$\vec{J} = \vec{L} + \vec{S} \quad (2.4)$$

Where for a $q\bar{q}$ meson system, the spin is $\vec{S} = \vec{S}_q + \vec{S}_{\bar{q}}$.

Parity and C-parity are two important operations in quantum mechanics. Parity operation reverses the momentum of a particle, but conserves the direction of the spin. If the spatial part of the system is conserved under the parity transformation, the assigned parity value to it is “+”, and if the system is antisymmetric under this transformation, the assigned parity is “-”. For a $q\bar{q}$ meson system, total parity is $P = P_q P_{\bar{q}} (-1)^L$. For a meson system, if the quark and the anti-quark are in a state with orbital angular momentum L, its parity value can be given through $P = (-1)^{(L+1)}$.

The C-parity operation transforms particles to their anti-particles, conserving the direction of the spin. For a system that is a combination of bosons, C is $(-1)^L$, while for a system of fermions, C is $(-1)^{L+S}$. So, for a $q\bar{q}$ meson system, $C = (-1)^{L+S}$ [6].

In the simple quark model only specific quantum numbers are allowed for a $q\bar{q}$ meson, such as $\{0^{-+}, 0^{++}, 1^{++}, 1^{+-}, 1^{--}, \dots\}$. Numbers such as $0^{--}, 0^{+-}, 1^{-+}$ and 2^{+-} are not allowed and are called exotic.

Tables 2.1 and 2.2 show the exotic and non-exotic quantum numbers for a $q\bar{q}$ state.

J	--	++	-+	+-
0	- - -	0 ⁺⁺	0 ⁻⁺	- - -
1	1 ⁻⁻	1 ⁺⁺	- - -	1 ⁺⁻
2	2 ⁻⁻	2 ⁺⁺	2 ⁻⁺	- - -
3	3 ⁻⁻	3 ⁺⁺	- - -	3 ⁺⁻
4	4 ⁻⁻	4 ⁺⁺	4 ⁻⁺	- - -
5	5 ⁻⁻	5 ⁺⁺	- - -	5 ⁺⁻

Table 2.1: Table shows the non-exotic $q\bar{q}$ mesons' quantum numbers [7].

J	--	++	-+	+-
0	0 ⁻⁻	- - -	- - -	0 ⁺⁻
1	- - -	- - -	1 ⁻⁺	- - -
2	- - -	- - -	- - -	2 ⁺⁻
3	- - -	- - -	3 ⁻⁺	- - -
4	- - -	- - -	- - -	4 ⁺⁻
5	- - -	- - -	5 ⁻⁺	- - -

Table 2.2: Table shows the exotic $q\bar{q}$ mesons' quantum numbers [7].

2.5 Exotic Mesons

There are different groups of exotic mesons. One group is called “tetraquarks” ($q\bar{q}q\bar{q}$). Another exotic meson group is called “hybrid mesons” ($q\bar{q}g$), which is combination of a valence quark, a valence anti-quark and a gluon. The third exotic group is “Glueballs” (gg), which has no valence quark or anti-quark. So far, there has been no unambiguous identification of any exotic meson's quantum numbers [8].

Since gluons possess color charge, they can interact with each other and form a glueball. Pure glueballs are difficult to identify because they mix with mesons, a phenomenon called “mixing”. According to the basics of quantum mechanics, each state of particles is a linear superposition of all the mass eigenstates that possess the same quantum numbers. Since light glueballs have the same J^{PC} values as conventional mesons, due to mixing, uncertainties arise to experimentally identify

them.

J_g	$S_{q\bar{q}}$	J^{PC}	Type	SampleMembers
1	0	1^{++}	conventional	a_1, f_1, f_1'
1	0	1^{--}	conventional	ρ_1, ω_1, ϕ_1
1	1	0^{-+}	conventional	π_0, η_0, η_0'
1	1	0^{+-}	exotic	b_0, h_0, h_0'
1	1	1^{-+}	exotic	π_1, η_1, η_1'
1	1	1^{+-}	conventional	b_1, h_1, h_1'
1	1	2^{-+}	conventional	π_2, η_2, η_2'
1	1	2^{+-}	exotic	b_2, h_2, h_2'

Table 2.3: Eight nonets of hybrid mesons.

The lightest exotic glueball will possibly have a mass of $4 \text{ GeV}/c^2$ and $J^{PC} = 2^{+-}$. Gluballs have been predicted in different QCD models, including bag models, constituent glue models, flux tube models, QCD sum rules and lattice gauge theory (LGT) [9].

The hybrid mesons are mesons with gluonic excitations. Table 2.3 shows the eight predicted nonets of hybrid mesons. In the flux-tube model, all eight hybrid nonets are degenerate with a mass of about $1.9 \text{ GeV}/c^2$, which is the mass of the lightest $J^{PC} = 1^{-+}$ exotic hybrid [10]. Due to few features of hybrid mesons, it is easier to detect hybrid mesons than glueballs.

2.6 Meson Spectroscopy

Mesons can be produced by the interaction between a target nucleon and pion (π), kaon (K), or photon (γ) beams. In case of using pion and kaon probes, in order to produce exotic mesons, a spin-flip in the entrance channel is required; as such, the

production of exotics is expected to be strongly suppressed. So in order to produce exotic mesons in an “one step” process, and study them, a high energy photon beam is required. Since photons, ω , ρ , and ϕ mesons have the same $J^{PC} = 1^{--}$ as shown in table 2.3, according to the mixing property, in a photon beam there is a probability of co-existing virtual ω , ρ , and ϕ mesons. A photon interacting with a nucleon would produce a proton or a neutron with the production of mesons, and this is a hadronic process. Also, since in a strong interaction, parity, C-parity, and isospin are conserved, knowing the initial and final states allows to determine the intermediate states through the use of the Partial Wave Analysis (PWA) technique, which gives us information about the intermediate hybrid mesons. The main aim of GlueX is to map the spectrum of these hybrid mesons in detail.

Chapter 3

The GlueX Detector

3.1 Introduction

The spin polarized 12 *GeV* electron beam, controlled by a series of steering magnets, will impinge on a diamond wafer of approximately 20 μm thickness and will generate coherent Bremsstrahlung radiation photons. The scattered electrons will be steered away from the photon beam by using a dipole magnet and its focal plane will be instrumented to provide the energy information required to “tag” the associated photons. The dipole magnet and its focal plane instrumentation constitute the “tagger” for GlueX.

The special orientation of the diamond crystal causes the Bremsstrahlung photons to be linearly polarized. In fact, 40% of the photons will be linearly polarized and will have energy range of 8-9 *GeV*, impinging on the GlueX detector [11]. The photons passing through the detector without interacting will be collected by the photon

beam dump. The GlueX detector has a hermetic (nearly 4π) coverage, and its main parts are shown in figure 3.1:

- * The target, which is liquid hydrogen, contained in a 30-*cm*-long vessel.
- * The Barrel calorimeter (BCAL) which will be used to measure the energy and emission angles of all incident particles. Its main role, however, is the detection and determination of the four momentum of photons in the 11° - 126° polar angle region (See figure 3.3).
- * The Forward Calorimeter (FCAL), which is a circular planar lead glass array. FCAL together with the BCAL provide the information on the 4-momentum of the detected photons.
- * The Time Of Flight wall (TOF), which is located immediately in front of the FCAL to provide timing information and charged particle identification at small angles (less than 11°).
- * Superconducting solenoid magnet, which provides a magnetic field of strength of 2.2 *T*, and surrounds most detectors.
- * The start counter, a series of plastic scintillator strips surrounding the target to provide beam bucket timing information.
- * The Central Drift Chamber (CDC), to track the particles with the polar angles between 20° to 170° coming from the target. The CDC surrounds the target.
- * The Forward Drift Chambers (FDC), which are disk-shaped drift chambers. Four packages are positioned in the forward region. The FDC and CDC, both are for tracking purposes [12, 13, 14].

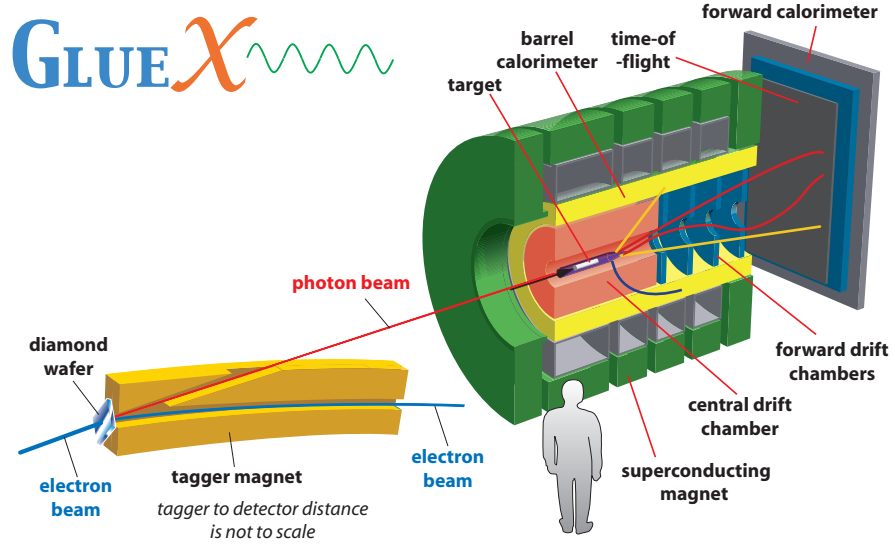


Figure 3.1: GlueX detector at Hall D contains several main parts. (original in color)

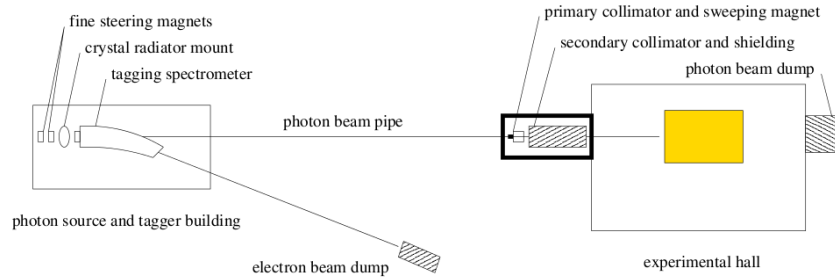


Figure 3.2: Schematic view of the photon beam. The objects are not to scale. The photon beam spot on the target will have a 2.5 cm radius [11]. (original in color)

3.2 BCAL

According to the detection mechanism employed, electromagnetic calorimeters are of several different types. Among those, a commonly employed design is that of sampling calorimeter, in which only a small fraction of the deposited energy is actively detected (sampled), with the remainder deposited in the insensitive/inert volume consisting usually of a high atomic number material. The BCAL is such a device [15].

The BCAL is 390 *cm* long, with an inner radius of 65 *cm* and an outer radius of 90 *cm*. The BCAL consists of 48 separate trapezoidal shaped modules as shown in figure 3.3, built at the University of Regina and shipped to Hall D, at JLab. The BCAL is positioned immediately inside the 2.2 *T* solenoid, and the barrel shape is the best shape to provide a coverage close to 4π for fixed target experiments. The BCAL's main goal is to detect the photons, which come from the decay of π^0 's and η 's, and to measure their energies and incident angles.

As shown in figure 3.3(b), the relative position of the target within the BCAL was chosen to maximize the effective detection solid angle given the Lorentz boost of the center of mass frame with respect to the laboratory frame. Each module of BCAL is made up of 15,350 of 1-*mm*-thick SCSF-78MJ scintillating fibers made by Kuraray¹, and layers of swaged 0.5 *mm* thin lead sheets. Each layer of lead contains grooves along its length to host the fibers. All these layers are glued together using optical epoxy², which has nearly the same index of the refraction as the inner (first) cladding layer of fibers, $n = 1.49$. Figure 3.4 shows the end view of a small part of a module showing the fibers.

¹Kuraray CO. LTD. Ote Center Building 8F, 1-1-3 Otemachi, Chiyoda-ku, Tokyo 100-8115, Japan. The agency in U.S.A.: Kuraray America, Inc. 4 Park Plaza, Suite 530, Irvine, CA 92614.

²Bicron BC-600 optical cement, Saint-Gobain Crystals & Detectors (<http://www.saint-gobain-northamerica.com>)

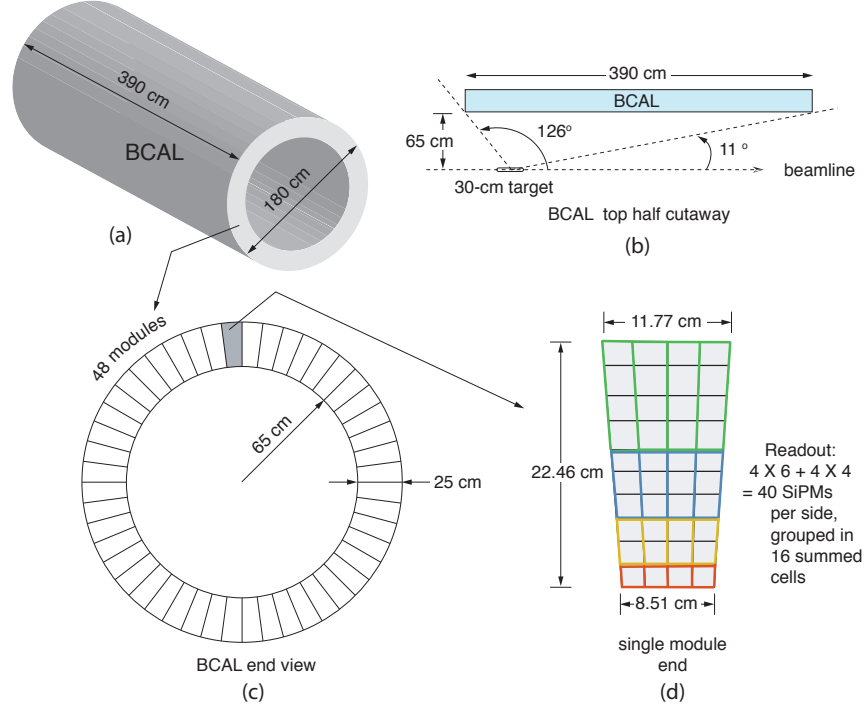


Figure 3.3: Sketch of Barrel Calorimeter readout. (a) BCAL schematic; (b) a BCAL module side view; (c) end view of the BCAL showing all 48 modules and (d) an end view of a single module showing readout segmentation in four rings (inner to outer) and 16 summed readout zones. (original in color)

Each end of a module will be viewed by 40 novel photosensors, as shown in figure 3.3(d), to provide energy and time measurements. These photosensors are commonly called Silicon PhotoMultipliers (SiPMs). Thus, in total, each module has 80 of these photosensors.

3.2.1 Scintillating Fibers

Three important properties of the scintillating material (scintillating fibers in BCAL) make them efficient for the GlueX experiment: sensitivity to energy, time of response, and pulse discrimination. The fibers used in the BCAL are double clad fibers, having

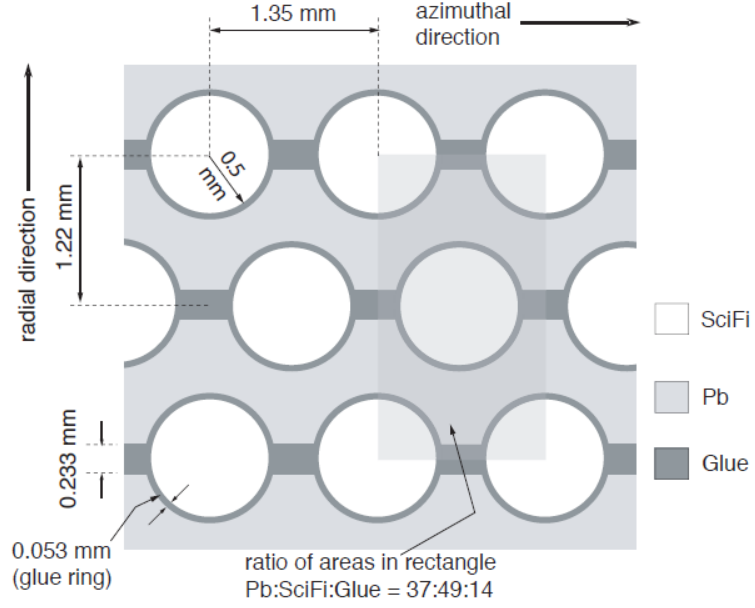


Figure 3.4: End view of a small section of a BCAL module.

three sections. The first is a scintillating core and the other two are layers of cladding. A double clad fiber is shown in figure 3.5. The first cladding is 0.03 *mm* thick with the index of refraction of $n = 1.49$, the second cladding is 0.01 *mm* thick, with an index of refraction of $n = 1.42$, and the core of the fiber has an index of refraction of $n = 1.60$. The presence of double cladding increases the number of detected photoelectrons in the photosensors by increasing the photon trapping efficiency. For a double clad fiber, compared to a single clad fiber, the capture increase of the photons is over 50% [16]. Thus there would be a similar increase in the detected photoelectrons. This results in better timing and energy resolutions, particularly at lower photon energies. The attenuation length of double clad fibers is equal to single clad fibers using the same combination of materials [16].

The analysis of a 2006 beam test of a BCAL prototype module yielded an energy resolution of $\sigma_E/E = 5.4\%/\sqrt{E(\text{GeV})} \oplus 2.3\%$ and time, difference resolution of

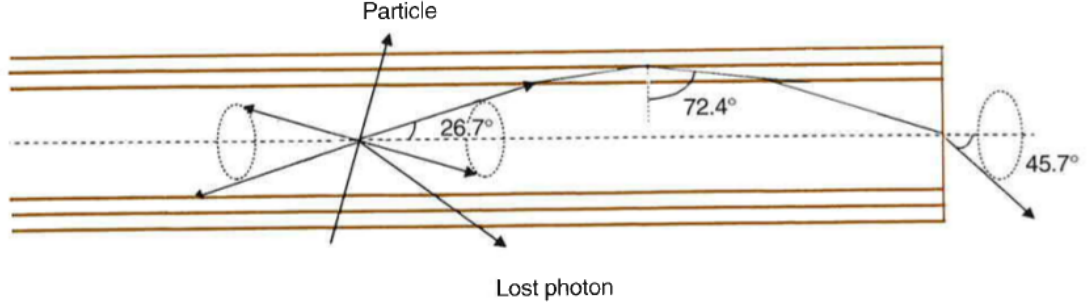


Figure 3.5: Graphic schematic of the critical angles in a double clad fiber [16]. (original in color)

$\sigma_{\Delta T/2} = 70ps/\sqrt{E(GeV)}$ [9]. These numbers indicate that the fibers used in that test (Pol. Hi. Tech. 044) met the project specification. The Kuraray fibers chosen for the production of the BCAL are superior to these in terms of light production, collection, and propagation.

3.2.2 BCAL Readout

Photons will travel the length of the scintillating fibers and then will be detected by the photosensors at the ends of BCAL's modules. To accommodate the 40 photosensors within the same area on each end of each BCAL module, GlueX will use trapezoidal light guides. Thus, for each SiPM, there will be a light guide, which will be directly glued to the face of a BCAL module. As seen in figure 3.6, immediately after each light guide there would be a SiPM placed with a 1 mm air gap in between of the SiPM and the light guide. The whole BCAL readout system will be in Nitrogen N_2 gas to provide a dry environment and avoid condensation on the electronics. A 3D rendering and electronics board are shown in figure 3.7.

The SiPM needs to be cooled down to 5° C to reduce the dark noise, by means of

chilled coolant mixture, cooling plates, cooling pipes and heat spreader as shown in figure 3.6.

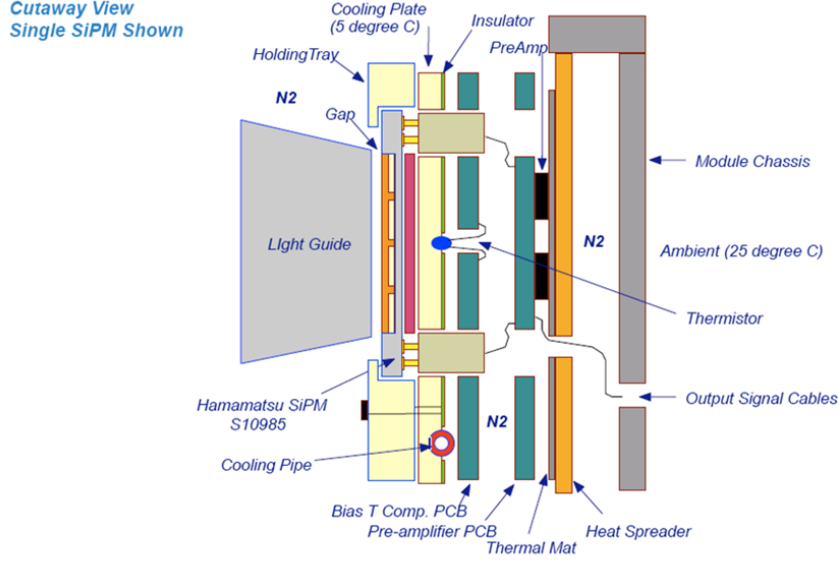


Figure 3.6: Light guides will be attached to the BCAL modules while the SiPMs will be held at the ends of the light guides with a 1 mm gap in between [17]. (original in color)

A common way to detect photons is to use conventional photomultiplier tubes (PMT), based on the photoelectric effect. A 2.2 T solenoid surrounds the BCAL, and since the PMTs are not immune to the magnetic field, PMTs cannot operate in such an environment (figure 3.8). On the other hand, SiPMs are immune to magnetic fields, and in some cases they have higher photon detection efficiency, lower cost, and are more compact and robust [18]. As an additional advantage, they do not require high voltage, which for PMT's is around 2,000 V, since SiPMs operate at around 70 V.

Each BCAL module is divided into two parts, the inner part and the outer part. The inner part of each BCAL module at each end contains 24 photosensors, grouped

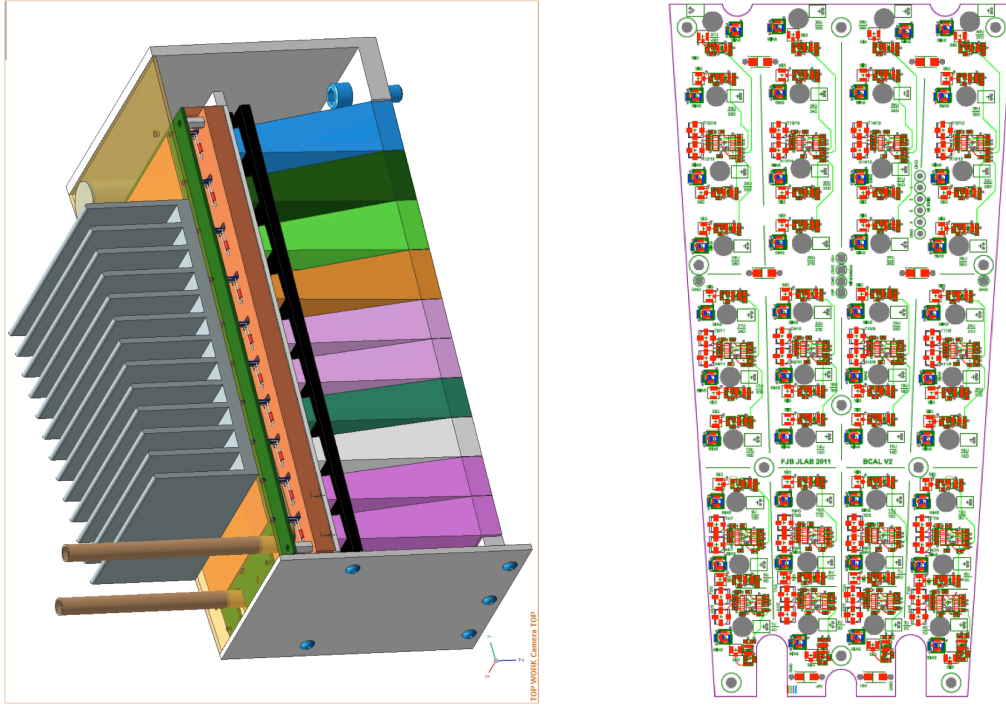


Figure 3.7: Left: A 3D rendering of figure 3.6. Right: Picture of a board containing all 40 SiPMs for one side of one module. (original in color)

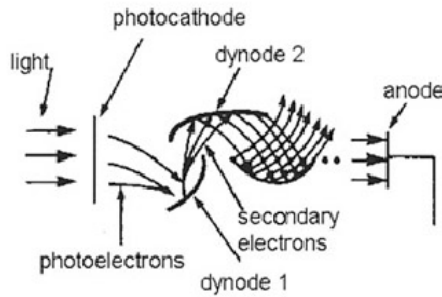


Figure 3.8: Design of a simple PMT. A PMT contains a photocathode, an anode, and several dynodes. The photoelectrons can easily be bent away and lost due to presence of any external magnetic field.

into three electronic readout (towers), to capture the early electromagnetic shower and to reach the required spatial and energy resolution. The outer part contains 16 of these photosensors grouped into four electronic readout towers as shown in

figure 3.7, to measure any remaining energy deposited in the BCAL. In order to maximize the photo statistics of light collection, it is desired to have a high photon detection efficiency of the photosensors.

Chapter 4

Silicon PhotoMultiplier Basic Function

4.1 Introduction

The SiPM is also known as solid state photomultiplier (SSPM), multi-pixel photon counter (MPPC), AMPD, MRS APD, G-APD, etc. It consists of an array of limited Geiger-mode Avalanche PhotoDiodes (APDs) on a silicon substrate [19, 20, 18]. These silicon APDs are of micron size, from $20\ \mu m$ to $100\ \mu m$. In other words, SiPMs consist of a matrix of typically thousands of independent micro-cells (pixels) per mm^2 , which are connected in parallel [21]. Commercially available SiPMs have areas of $1 \times 1\ mm^2$ or up to $3 \times 3\ mm^2$. The required area for each SiPM for GlueX is considerably larger ($1.2 \times 1.2\ cm^2$). Such devices were first developed by SensL¹

¹6800 Airport Business Park, Cork, Ireland (<http://sensl.com/>)

and subsequently by Hamamatsu². Hamamatsu, a photonics company in Japan, has been selected to manufacture the specified SiPMs for GlueX, following a tender-and-bidding process [22]. SiPMs have applications in many different fields such as high energy physics calorimetry, astrophysics or medical imaging [23, 24, 25].

4.2 Avalanche PhotoDiodes

The APDs, which are based on the process of impact ionization, in contrast to PMTs, are solid state devices based on a p-n junction. Initial electrons will be produced due to the photoelectric effect by the incident photons. These photoelectrons gain higher velocity due to the presence of an external electric field (breakdown voltage for APDs), and if the energy gained by the electrons in this duration is high enough, it will free one or more secondary electrons from the molecules. This process is called impact ionization in which the initial electrons will impart their energy to the molecules to create more free electrons. Thus, the energy of the traveling electron should be equal or more than the band gap energy of the material (SiO_2 for the SiPMs). This specifies the magnitude of the external voltage that has to be applied.

The secondary electrons also experience the same external electric field, and therefore they will also produce more electrons and so on. Eventually this process makes avalanche multiplication of charge pairs, and thus there would be an electric current. This current is related to the number and energy of the incident photons. Thus APDs are based on avalanche multiplication, and due to impact ionization they have

²HAMAMATSU Photonics K.K., 325-6, Sunayama-cho, Naka-ku, Hamamatsu City, Shizuoka Pref., 430-8587, Japan (<http://www.hamamatsu.com/>)

internal current gain effect. The avalanche is limited by the choice of a quenching resistor that controls final gain.

In figure 4.1 the avalanche current and the breakdown voltage are shown for an APD. When the temperature is increased the breakdown voltage is decreased.

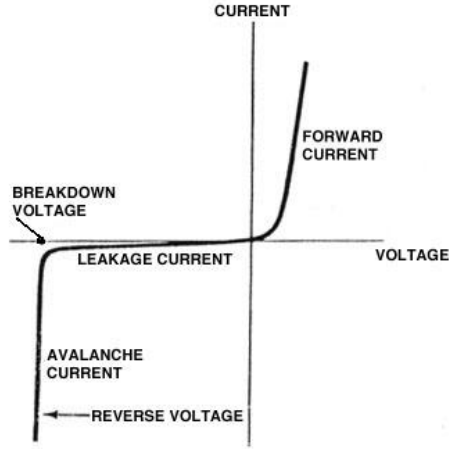


Figure 4.1: The breakdown voltage and the avalanche current for an APD are acted in reversed voltage.

Figure 4.2 shows a design of a simple avalanche photodetector. An APD consists of an intrinsic p-type material (or slightly doped p-type material) which is located between a heavily doped p-side and a heavily doped n-side as shown in figure 4.2. The incident radiation passes through the intrinsic material (or R_{abs} as shown in figure 4.3), and produces electron-hole pairs along its path.

The electrons move toward the p-region, and thus the R_{mult} , as shown in figure 4.3, is the region that the charge multiplication happens [26]. This avalanche of electrons is called a Geiger-type discharge.

The voltage above the breakdown voltage is called overbias voltage. The avalanche of the electrons would increase with the increase in overbias. If the bias drops below

the breakdown voltage by an external resistor, the avalanche can be stopped, and these APDs are said to operate in limited Geiger mode.

4.2.1 APD Gain and Quantum Efficiency

The gain for an APD is as follows:

$$G = \frac{C \cdot (V - V_{br})}{e} \quad (4.1)$$

Where G is the gain, e is the charge of an electron, C is the APD capacitance, and $(V - V_{br})$ is the overbias [27].

Quantum Efficiency (QE) of an APD is an important factor showing how well the APD absorbs the incident photons and produces charge carriers.

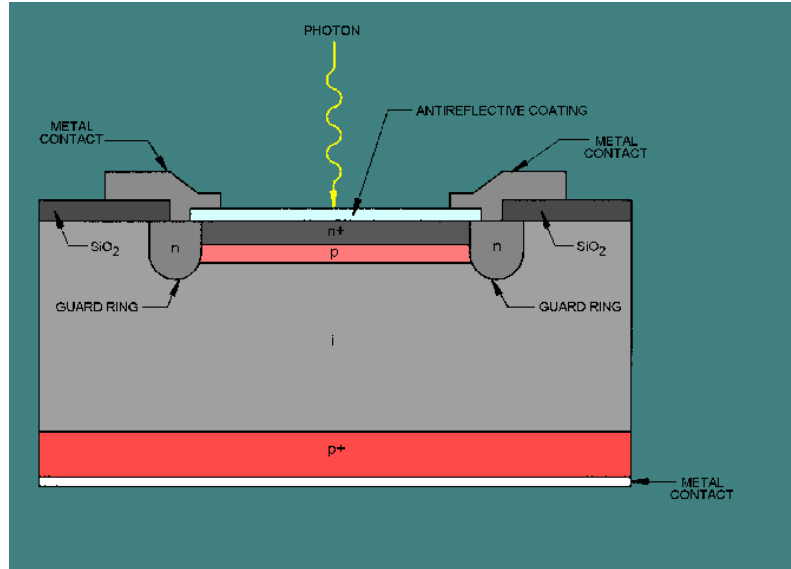


Figure 4.2: Basic structure of an APD [28]. (original in color)

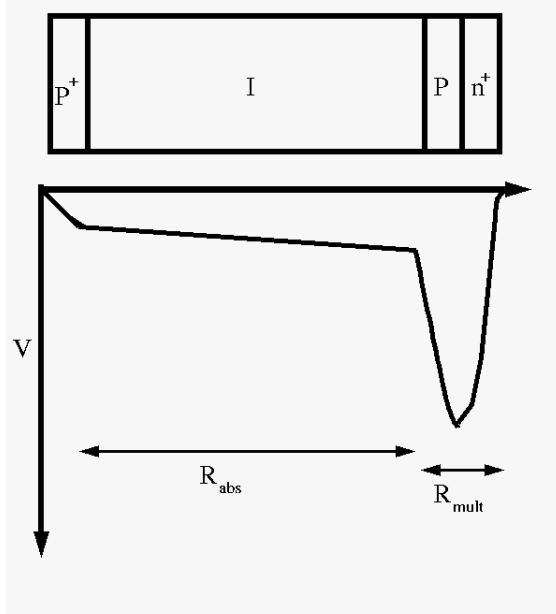


Figure 4.3: The structure for a simple APD and the electric field profile of the structure.

4.3 Silicon Photomultipliers

Each silicon APD in a SiPM is referred to as a pixel and is a binary element. When an APD starts the Geiger avalanche it is in “on” state. Thus, the output of each APD is a digital signal. The output of all of these signals would be summed together and form an analog signal, which can be seen on an oscilloscope screen. Figure 4.4 shows an output signal from a Hamamatsu SiPM. The avalanche in these APDs is quenched by a silicon resistor, which is in series with the Pixel [29, 30]. Each pixel is coupled to an aluminum conductor which carries the resulting current from all the avalanches. SiPMs, like any other light detectors, have different types of noise associated with their operation.

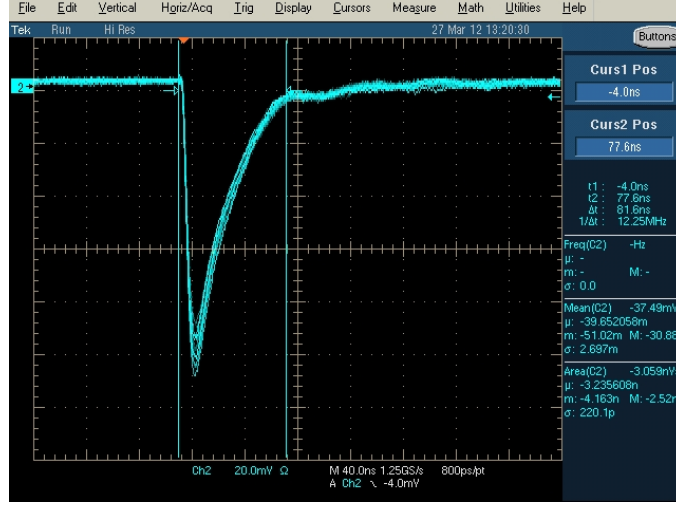


Figure 4.4: The pulse of a SiPM units, using the laser as the light source. The oscilloscope is able to provide the area of the pulse. The pulse height shown (y-axis) is about 100mV with around 80 ns timing base (x-axis). (original in color)

4.4 Photon Detection Efficiency

The ratio of the number of pixels fired, or number of registering photons, in a SiPM device, over the number of incident photons is called the photon detection efficiency (PDE). Typical SiPMs have a PDE range of $10 - 25\%$. The PDE of a SiPM depends on several factors, including intrinsic quantum efficiency of a pixel ($QE(\lambda)$), avalanche probability (α_p), and the fraction of photosensitive surface to the total geometric area of the detector presented to the incident photon flux, which is called the geometric fill factor (F). PDE is given as:

$$PDE(\lambda, \Delta V_{br}, T) = QE(\lambda) \cdot F \cdot \alpha_p(\lambda, \Delta V_{br}, T) \quad (4.2)$$

where λ is the wavelength of the incident photons, and ΔV_{br} is the overbias (voltage above the breakdown voltage) [31, 18].

In fact, Q_E is the quantum efficiency of the silicon APDs, which is the ratio of

the photons that excite an electron-hole pair in the APD to the total number of incident photons. APD quantum efficiency is dependent on the wavelength of the photons. Since the energy of a photon is related to its wavelength ($E_\gamma = \frac{hc}{\lambda}$), different photons with different energies (wavelengths) have different probabilities of exciting the electron-hole pairs. Thus, the quantum efficiency of a pixel (APD) depends on the incident photon's wavelength. The QE for a Hamamatsu APD array for incident photons of wavelength 420 *nm* and at room temperature is about 60 – 70% [32]. Avalanche probability depends on the operational bias; when an electron-hole pair is excited by the registered photon, the probability of initiating a self-sustaining avalanche in the APD is $\alpha_p(\Delta V_{br})$. When the overbias voltage is increased, the electric field in the APD is increased and will increase the kinetic energy of the photoelectron and thus the probability for the avalanche will increase.

4.4.1 Fill Factor

Figure 4.5 shows an array of silicon APDs connected together. As shown in the figure, silicon APDs are arranged with barriers in between them to reduce the cross talk. A space is required, as well, for the quenching resistance. Therefore, each array of SiPMs, and also each pixel, have some inactive space. For Hamamatsu APDs the reported fill factors is around 60% [33].

4.5 SiPM Noise

For SiPMs, the two main types of noise are dark current and cross talk. These are discussed below.

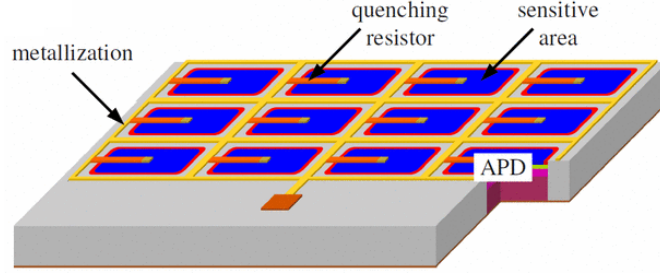


Figure 4.5: Array of APDs [34]. (original in color)

4.5.1 Dark Current

Dark current for PMTs is mainly due to the thermionic emission of electrons from the photocathode. It also can be due to the ionization of the residual gases inside the PMT tube [27].

The main source of noise for SiPMs is the dark current. Dark current in SiPMs is mainly due to electrons being generated thermally in the p-n junction depletion region. These will cause an avalanche, and the APD will be in an “on” state and a “photon” will be counted, resulting in a current even in the absence of light. Dark current in SiPMs cannot be avoided but it can be reduced. The dark current of a SiPM can be decreased by a factor of 10, if its temperature is reduced by 20 °C [27].

4.5.2 Cross Talk

Cross talk is another source of non-linearity in SiPMs. This is the result of grouping of many pixels in a small area. Electrons travel through materials naturally and interact with that material and thus produce new photons. In a SiPM, since its pixels are adjacent, excited electrons can travel from one pixel to another, resulting in undesired avalanches from a single photon. One way to reduce the cross talk is to erect optical barriers between pixels, called “trenching”.

4.6 Recovery Time

After each pixel is “fired” and the avalanche starts it needs certain time to recover to its initial state, when it will be sensitive to photons again. Mostly the pixel’s recovery time is 50 *ns*, which leads to a count rate limit of 20 *MHz* [35]. So for a SiPM composed of many APDs, if all the APDs are triggered at the same time, then the count rate is 20 *MHz*. However, that is not normally the case, and the pixels do not fire at the same time. Thus, the rate will be less than 20 *MHz* and will be determined by the saturation condition.

4.7 Linearity

For a SiPM device linearity is desired, which means that the number of incident photons should be proportional to the output signal or current. In other words, it is desired that for each pixel, one and only one photon starts the avalanche of that pixel. The output current of the SiPM is as follows:

$$I = \frac{dN_\gamma}{dt} \cdot PDE \cdot G \cdot e \quad (4.3)$$

Where N_γ is the number of incident photons, PDE is the photon detection efficiency, G is the gain, and e is the charge of an electron.

If a pixel receives more than one photon within its recovery time, then the SiPM’s output is not proportional to the number of incident photons and the linearity of the response is lost. Therefore, as the intensity of the photon flux increases the probability of loss of linearity will increase as well. Cross talk is another factor that

reduces the probability of linearity. The specification for the GlueX BCAL readout require better than 10% linearity [27].

4.8 Dynamic Range

For a SiPM, it is expected that:

$$\frac{N_{\gamma} \cdot PDE}{m} < 1 \quad (4.4)$$

Where m is number of pixels. Equation 4.4 is due to the fact that only one photon at a time can be counted by an APD. The dynamic range of a SiPM must be greater than the maximum number of photons expected to reach the SiPM.

The maximum number of photons reaching a SiPM for the GlueX BCAL is estimated to be around 30,000 photons, and since the chosen SiPMs have about 50,000 pixels each, and the PDE is more than 20%, the SiPMs have a dynamic range of $N_{\gamma} < 250,000$ photons [27].

Chapter 5

Gain Uniformity of the 2010 and the 2011 SiPM Units

5.1 Introduction

Among the two available Hamamatsu 2010 SiPM units at the University of Regina, one was chosen, in addition to the 10, 2011-pre-production units, and gain uniformity tests were carried out for all the eleven units. These SiPMs consist of 16 of 3×3 mm² cells as shown in figure 5.1. The aim of these tests was to investigate the gain uniformity of the 16 cells, in other words to examine the degree of non-uniformity in the output pulse height of these cells.

Each cell was also divided into 4 sub-cells as shown in figure 5.1, thus the gain uniformity within a cell could be studied in finer detail.

As shown in figure 5.1, based on each sub-cell's geometry, the sub-cells were divided into different groups or families (indicated by the different colors) that will be discussed later.

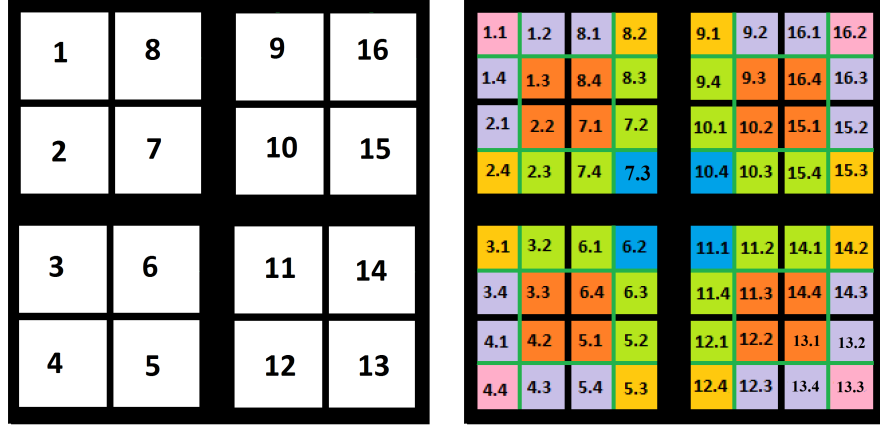


Figure 5.1: The 16 cells of the SiPM (left) and the 64 sub-cells are shown. The numbers correspond to the cell or sub-cell identification. (original in color)

5.2 Gain Uniformity Set-up

The list of equipment used for the gain uniformity is shown bellow:

1. Pulsed UV LED.
2. x-y scanner, Zaber Technology¹ T-L S28-I, Serial No: 4064.
3. A same type of scintillating fiber that is used in the BCAL, which is connected to the LED at one end, and is pointing to the SiPM at the other end. The end of the fiber is connected to a 1.48 *cm* long collimator, made out of black polyethylene plastic, with an aperture of 1 *mm* diameter.
4. Two power supplies for the pre-amplifier voltage (DC Regulated Power Supply

¹Zaber Technologies Inc., 1st Floor, 1777 West 75th Ave, Vancouver, British Columbia, Canada, V6P 6P2 (<http://www.zaber.com/>)

CSI²3003 XIII, and Regulated DC Power Supply GP³-1503).

5. A computer to manage the scanner's movement.
6. 6487 Keithley⁴ Picoammeter/Voltage Source for the bias voltage.
7. Tektronix⁵ TDS 5104 Digital Phosphor Oscilloscope.
8. A dark box to put the scanner in it and do the test, to assure as much extraneous light elimination as possible.

The SiPM has one summed output for all the SiPM cells. Therefore, the setup allowed for the illumination of each cell individually, by positioning the fiber with its collimator directly in the middle of the cell under investigation. The collimation ensures that light does not reach neighboring cells.

5.3 Gain Uniformity Result

The X-Y scanner was programmed to scan the whole area of the SiPM in several different ways: “Forward Scan”, “Backward Scan”, “Random Scan”, and “Cell Mapping”. For each test the LED was warmed up for more than 20 minutes, and each test was done at room temperature ($\approx 23^\circ\text{C}$). The pulse height from the SiPM was viewed on the oscilloscope for a few (approximately 30-60) seconds to ensure stability, and the recorded value indicates the average. For the 2010-pre-production SiPM units the pre-amplifier voltages were $+2.17\text{ V}$ and -5 V , and the operating voltage was $+70.79\text{ V}$, with 0.9 V overbias.

²Circuit Specialists, Inc, 220 South Country Club Drive Mesa, AZ 85210, United States (<http://www.circuitspecialists.com/>)

³5 F., No.350, Sec. 2, Zhongshan Rd., Zhonghe Dist., New Taipei City, Taiwan, 235, R.O.C.(<http://www.glacialpower.com/>)

⁴KEITHLEY CORPORATE HEADQUARTERS, Keithley Instruments, Inc., 28775 Aurora Road, Cleveland, Ohio 44139 (<http://www.keithley.com/>)

⁵Tektronix, Inc., 14150 SW Karl Braun Drive, P.O. Box 500, Beaverton, OR 97077, United States (<http://www.tek.com/>)

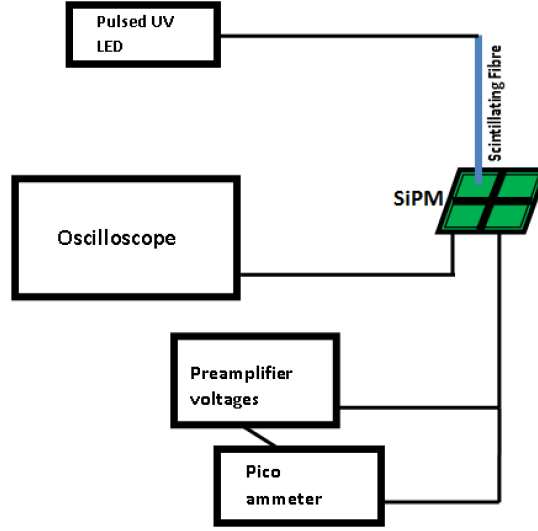


Figure 5.2: Gain uniformity test setup showing the fiber that transports the light from the light source. The fiber tip above the SiPM includes a 1-*mm* diameter plastic collimator. (original in color)

5.3.1 Forward Scan

In the forward scan mode, the scanner was programmed to scan the SiPM cells as shown in figure 5.3. So the scanned cell tags were: 1, 2, 3, 4, 5, 6, 7, 8, 9, 10, 11, 12, 13, 14, 15, 16, and 1. The scanner was programmed to point exactly at the center of each cell, and to return to the starting position in cell 1.

The results for the forward scan are shown in figure 5.5. These tests were done in two different days, and same temperature. The UV LED has a potentiometer knob used to set its bias and therefore its brightness. The knob has no gradation. Even though an effort was made to set it to the same approximate setting, differences occurred from one run to the next. However, on a relative scale of the 16 cells within a single run, such differences do not matter. Although pulse heights were not the same for each test run, the relative pulse height of the 16 cells was almost the same for the three different tests.

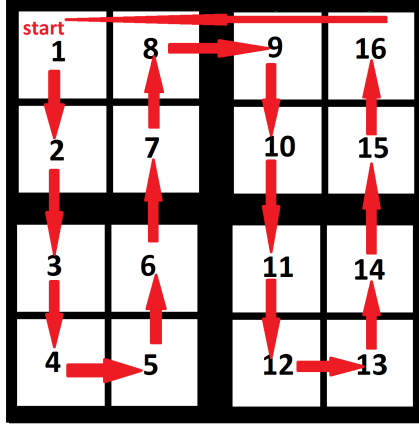


Figure 5.3: Forward scan, path of the X-Y scanner. (original in color)

5.3.2 Backward Scan

In the backward scan mode, the scanner was programmed to scan the SiPM cells as shown in figure 5.4. So the scanned cell tags were: 1, 16, 15, 14, 13, 12, 11, 10, 9, 8, 7, 6, 5, 4, 3, 2, and 1, respectively. As before, the fiber collimator was pointing to the centre of each cell, and returning to the starting position. The results for the backward scan are shown in figure 5.5.

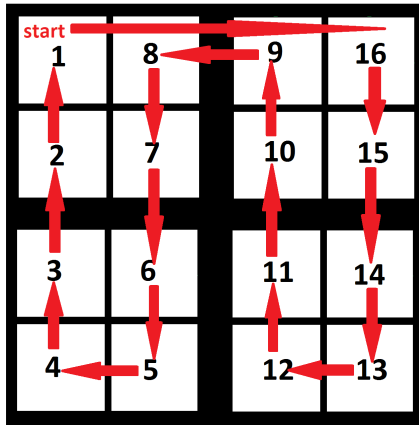


Figure 5.4: Backward scan, path of the X-Y scanner. (original in color)

5.3.3 Random Scan

In the random scan mode, the scanner was programmed to scan the SiPM cells in a nearly random fashion. The pattern was fixed for both of the separate days that the tests were carried out, but the scanner's movement was not in a sequential manner as it was for forward and backward scans. Therefore the cell tags in sequence were: 1, 7, 15, 4, 12, 3, 8, 6, 9, 2, 5, 16, 11, 13, 10, 14, 1. The scanner was also programmed to be pointing exactly at the center of each cell.

The results for the gain uniformity scans for the 2010 unit are shown in figure 5.5. The relative pulse heights of different cells are consistent with the previous results. Inspection of figure 5.5 shows that the relative gain of the cells is quite similar, with differences in a few cells at the 5% level (for the 2012 unit). Note that these three tests were conducted over a period of two weeks, in order to assure that variation in the building's power, changes in temperature at different days and etc. did not affect the experiment.

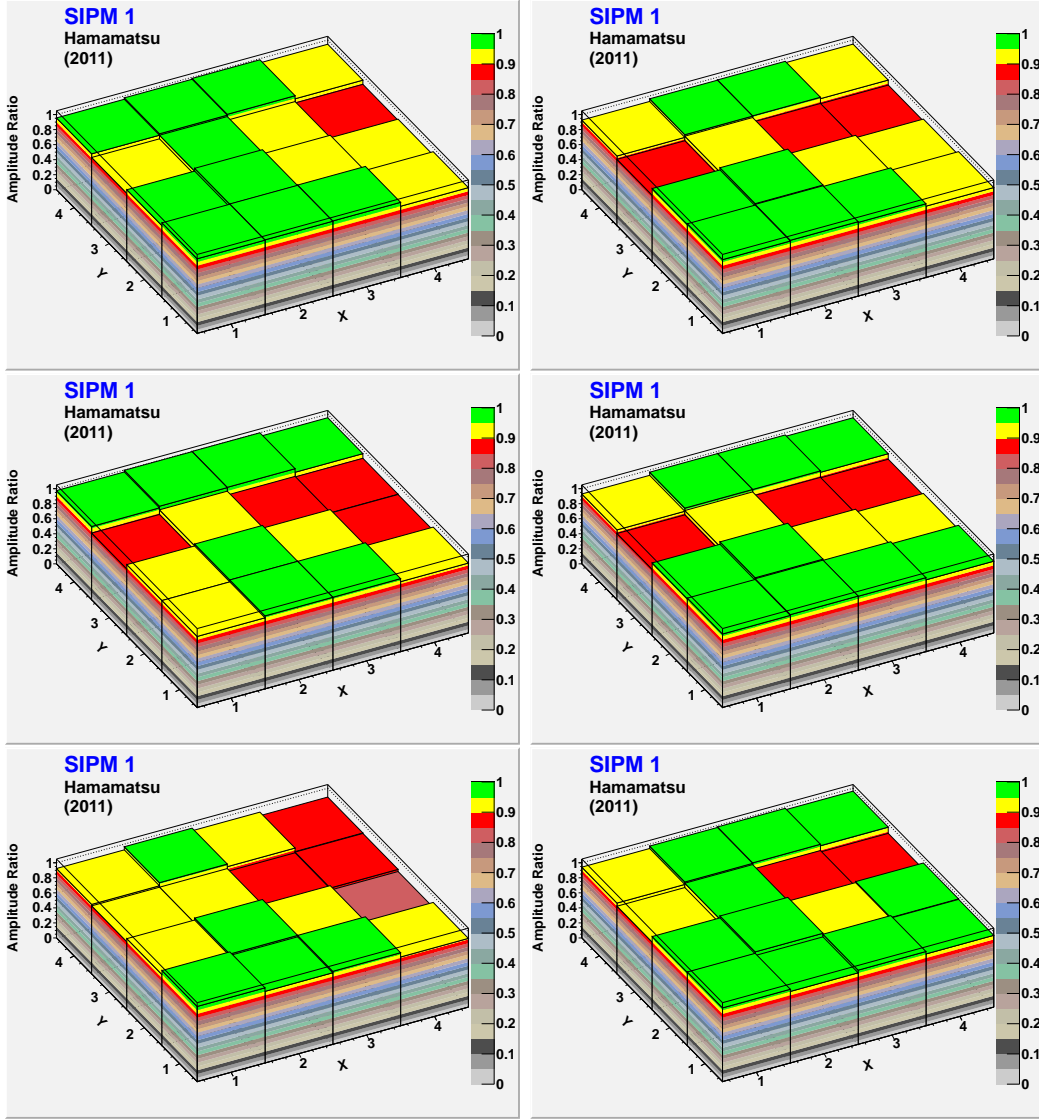


Figure 5.5: Gain uniformity scans for the 2010 unit, in a two dimensional representation. Top row: forward scans (left measured on March 28 and right on April 4, 2011.). Middle row: backward scans (left carried out on March 30 and right on April 11, 2011.) Bottom row: random scans (left carried out on April 4 and right on April 11, 2011.) (original in color)

5.3.4 Cell Mapping

To study if the gain is uniform within a cell, a cell was divided into four sub-cells and the gain of each of these sub-cells was studied. For this test, each cell is scanned four times, in four different locations of the same cell. In other words, each cell consists of four sub-cells, and in this test all the 64 sub-cells were scanned as shown in figure 5.6. The scanner is also programmed to be pointing at the center of each sub-cell. The results for this test are shown in figure 5.7.

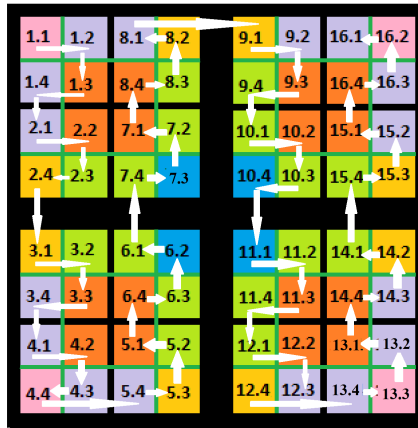


Figure 5.6: Cell mapping, path of the X-Y scanner. (original in color)

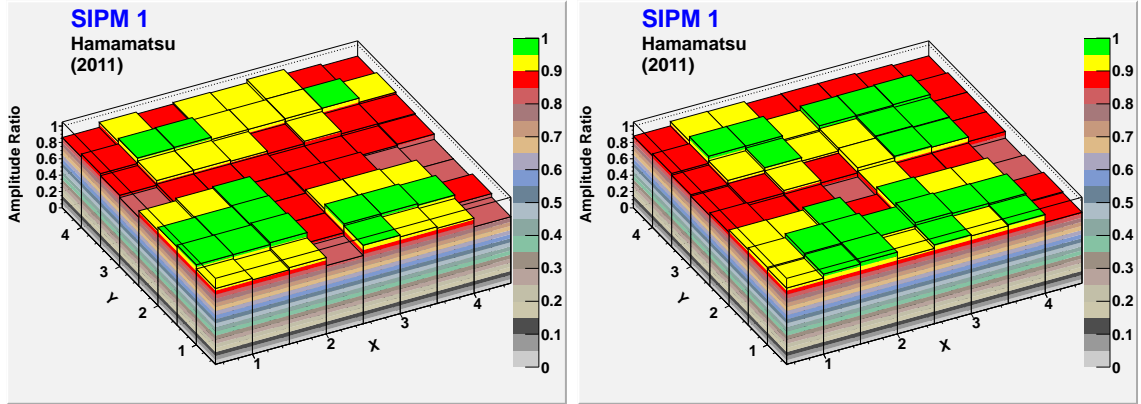


Figure 5.7: Gain uniformity for the 2010 unit, cell mapping, left: carried out on April 29, right: carried out on measured on May 3. Notice that an overall similar pattern emerges, as those shown in the $3 \times 3 \text{ mm}^2$ cell scans (forward, backward and random), as is shown in figure 5.5. (original in color)

5.4 Consistency Checks

To ensure the validity and repeatability of our measurements, we carried out a study of the stability of the LED and we tested the symmetry of the SiPM setup.

5.4.1 LED Investigation

We carried out measurements to ensure that the LED pulse is stable over time, and the result was positive. For this purpose, the LED was pointing at the center of a cell of the SiPM, for about six hours, the pre-amplifier voltages and the bias voltage were provided as described earlier. The SiPM pulse, which was a result of the LED pulse, was stable over the observation time, following the 10 minute warm up stage. Moreover, in all the measurements, the LED was warmed up for at least 20 minutes.

5.4.2 Sub-Cell Geometry Study

One purpose of this experiment was to find how efficient the collimator was in directing light to the SiPM. Thus it was assumed that the end of the fiber was not connected to a collimator and sub-cells were categorized into six groups or families based on their geometry with respect to their edges. Each family is shown in a different color in figure 5.9. For example, the middle four cells (colored orange) have other cells surrounding them on all sides, so that any light missing one of these cells would be captured by an adjacent one and thus recorded through the summed output. Likewise, the corner ones (colored pink) have adjacent cells only along two edges, and thus light may be lost across the other two edges, and so on. Each cell is $3 \times 3 \text{ mm}^2$, so each sub-cell is $1.5 \times 1.5 \text{ mm}^2$. The families are:

Family 1.1: {1.1, 4.4, 13.3, 16.2}

Family 1.2: {1.2, 1.4, 2.1, 3.4, 4.1, 4.3, 5.4, 8.1, 9.2, 12.3, 13.2, 13.4, 14.3, 15.2, 16.1, 16.3}

Family 1.3: {1.3, 2.2, 3.3, 4.2, 5.1, 6.4, 7.1, 8.4, 9.3, 10.2, 11.3, 12.2, 13.1, 14.4, 15.1, 16.4}

Family 2.3: {2.3, 3.2, 5.2, 6.1, 6.3, 7.2, 7.4, 8.3, 9.4, 10.1, 10.3, 11.2, 11.4, 12.1, 14.1, 15.4}

Family 2.4: {2.4, 3.1, 5.3, 8.2, 9.1, 12.4, 14.2, 15.3}

Family 6.2: {6.2, 7.3, 10.4, 11.1}

As mentioned earlier, although the end of the fiber was connected to a 1.48 *cm* long collimator with an aperture of 1 *mm* diameter, for this investigation it was assumed that no collimator was used, and a calculation was done to find how much active area would be illuminated when emitting light to the sub-cells.

Since the fiber's diameter is 1.0 mm and the space between the fiber and the SiPM is 1.6 mm , and the maximum angle that the light goes out of the fiber is $\alpha=45.7^\circ$, then according to figure 5.4 all the LED's light does not reach only one sub-cell. When the light reaches the SiPM it covers a circle with a radius of at least 1.6 mm , so the circle's diameter is larger than the sub-cell side. So, for some families the light will be absorbed by the other sub-cells, and for some families the light will be lost because of the SiPM's inactive area. Also, each cell has a different gain, so the families should not actually be compared to each other in an absolute sense. But if the SiPM is assumed to be an ideal one, and therefore each has the same gain as the other ones, then it is expected that the sub-cells in each family will have the same losses due to geometry. For example for the family 1.3 (i.e. sub-cells 1.3, 8.4, 2.2, 7.1, 3.3, 6.4, 4.2, 5.1, 9.3, 16.4, 10.2, 15.1, 11.3, 14.4, 12.2, 13.1), the expectation is that, if all cells had identical gain, the family 1.3 cells would exhibit the highest pulse height on the scope, since they would suffer no losses due to edge effects.

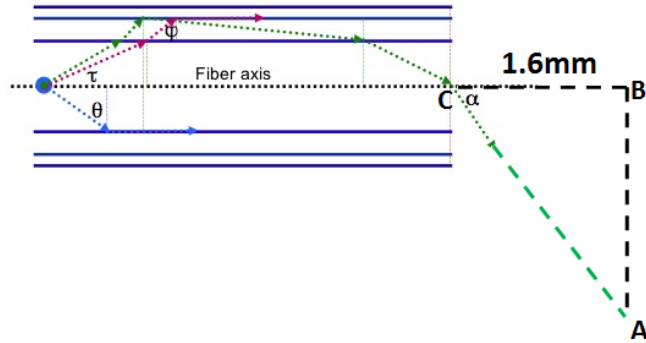


Figure 5.8: Illumination of sub-cells due to the distance between the SiPM and the fiber, in the absence of a collimator. The fiber core and claddings are shown schematically (not to the scale). (original in color)

The data from two separate tests of the sub-cell pulse heights are tabulated in tables 5.1 and 5.2. Table 5.1 shows the maximum, minimum, and average pulse height



Figure 5.9: Schematic view of the SiPM's sub-cell families. (original in color)

Family	Maximum Pulse Height(mV)	Minimum Pulse Height(mV)	Average (sub-cells' pulse heights in a family)	STDEV
1.1	-259 ± 9	-241 ± 6	-246	9
1.2	-278 ± 10	-236 ± 10	-256	11
1.3	-277 ± 7	-256 ± 6	-269	7
2.3	-277 ± 7	-239 ± 9	-257	12
2.4	-268 ± 8	-227 ± 7	-248	12
6.2	-264 ± 8	-233 ± 9	-249	13

Table 5.1: Sub-cell pulse heights for pulse 1.

of the sub-cells of each family, carried out on April 29, 2011. Table 5.2 shows the same information as table 5.1 for the cell mapping test carried out on May 3.

The result of studying these families is shown in figures A.1 and A.2 in the Appendix. The horizontal axis shows each sub-cell tag, while the vertical axis shows the percentage of pulse height, which is given as the difference of each sub-cell pulse height of each family from the average of that family, relative to this average.

According to figure 5.10, due to the area of the SiPM that the beam covers for each family, it is expected that the pulse height (assuming gain is the same) of each family

Family	Maximum Pulse Height(mV)	Minimum Pulse Height(mV)	Average (sub-cells' pulse heights in a family)	STDEV
1.1	-252 ± 9	-221 ± 9	-236	13
1.2	-266 ± 9	-218 ± 8	-246	12
1.3	-272 ± 9	-239 ± 9	-258	9
2.3	-267 ± 7	-227 ± 7	-246	12
2.4	-261 ± 9	-218 ± 8	-240	14
6.2	-243 ± 10	-232 ± 9	-238	5

Table 5.2: Sub-cell pulse heights for pulse 2.

follows the relation below: (Note that it is assumed that the fiber is not connected to the collimator at the end.)

$$1.3 > 2.3 > 1.2 > 6.2 > 2.4 > 1.1 \quad (5.1)$$

In figure 5.10 the blue circles show the area on the SiPM that the LED illuminates. As already discussed, the radius of the circle is 1.64 mm , and thus its area is $\pi \times r^2 = \pi(1.64)^2 = 8.45 \text{ mm}^2$. In other words, for sub-cells of family 1.3 the LED's light does not encounter any inactive area, and thus they will have the highest collection. But for other families some segments of the circle will be viewing the inactive area, and thus resulting in smaller collection. Although it seems that the assumption is true according to tables 5.3 and 5.1, but the differences are actually small and within the experimental error, thus, it cannot be concluded that the collimator being used is not a proper one. The differences might be due to the reflection and refraction after the light passing through the top layer of the SiPM. Thus studies show that the collimator makes the tests more reliable. More graphs on studying the SiPM unit are in Appendix A.

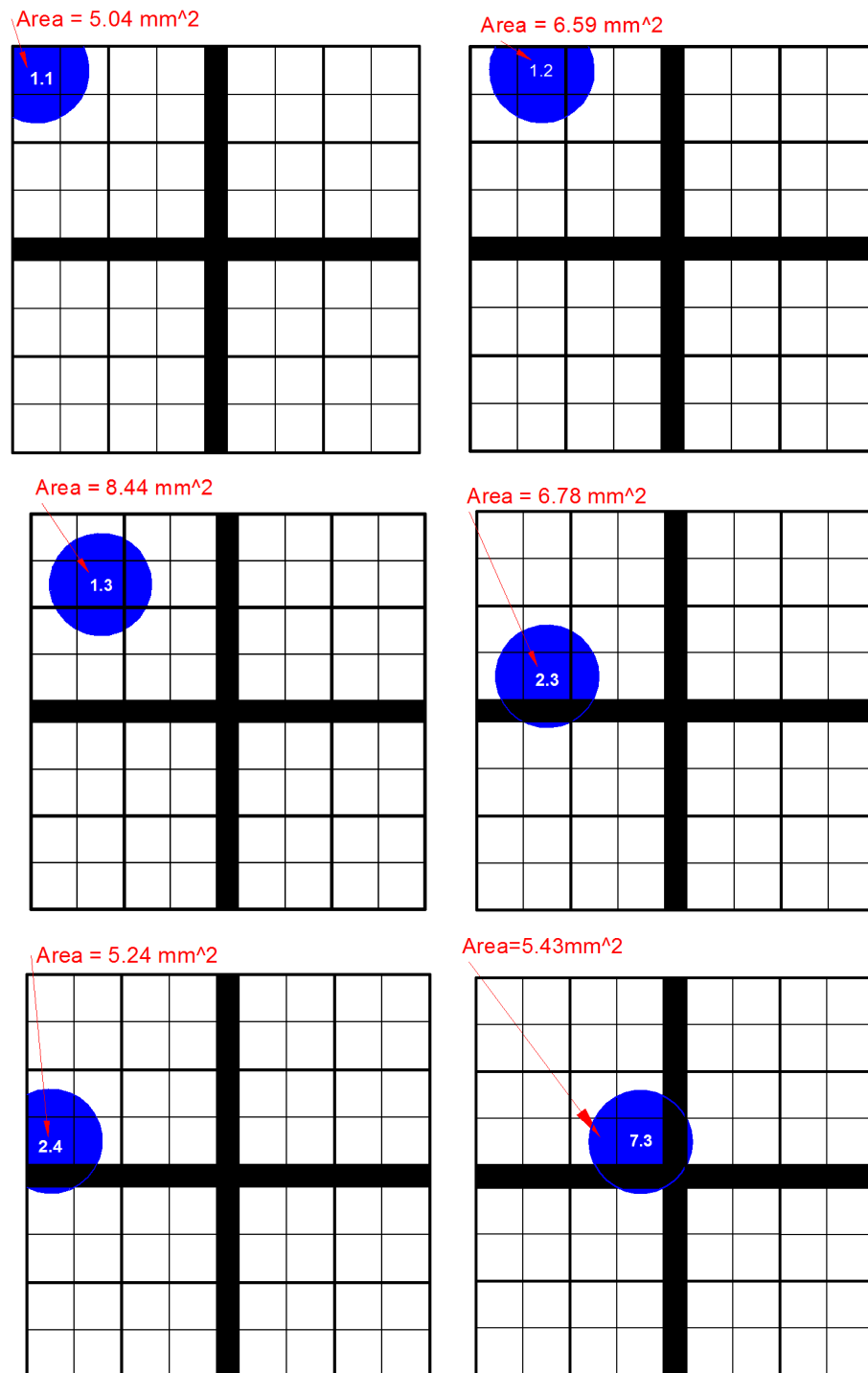


Figure 5.10: Fired active areas for different families (families 1.1, 1.2, 1.3, 2.3, 2.4, 6.2 or 7.3). (original in color)

Family	Average of Pulse 1 (mV)	Average of Pulse 2 (mV)
1.3	-269 ± 7	-258 ± 9
2.3	-257 ± 12	-246 ± 12
1.2	-256 ± 11	-246 ± 12
6.2	-249 ± 13	-238 ± 5
2.4	-248 ± 12	-240 ± 14
1.1	-246 ± 9	-236 ± 13

Table 5.3: Pulse height averages.

5.5 First Article Units (2011 Pre-Production SiPM Units)

5.5.1 Visual Inspection

The 10 SiPM pre-production units were received at the University of Regina, on Wednesday, June 15, 2011. Primarily, visual inspection was done as shown in table 5.4. Pin tags and side tags are shown in figure 5.11.

Serial #	Side 1 (mm)	Side 2 (mm)	Side 3 (mm)	Side 4 (mm)	Comment
75	20.00	14.90	20.00	14.90	Pin #4-2 bent
76	20.00	14.90	20.00	14.90	Pin #4-2 bent slightly
77	20.00	14.90	20.00	14.90	Pin #3-1 bent slightly
78	20.00	14.90	20.00	14.90	Pin #4-2 bent slightly
79	20.00	14.89	20.00	14.89	No obvious damage.
80	20.01	14.92	20.00	14.92	No obvious damage.
81	20.00	14.88	20.01	14.89	No obvious damage.
82	20.01	14.90	20.00	14.90	Pin #1-2 bent slightly
84	20.00	14.90	20.00	14.90	Pin #4-2 bent
85	20.00	14.90	20.00	14.90	Pin #4-1 bent slightly

Table 5.4: Visual Inspection of the 10, 2011-pre-production units.

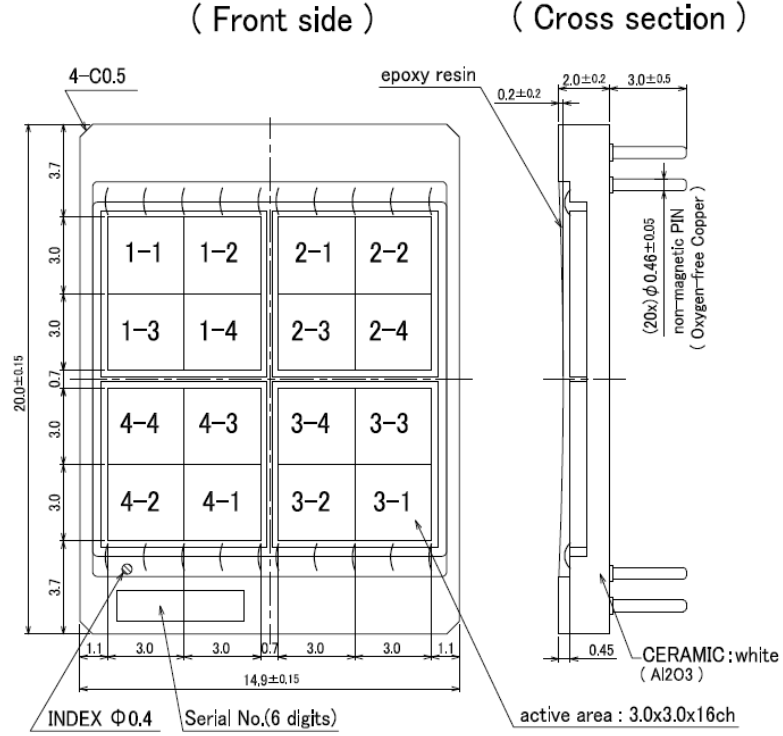


Figure 5.11: Schematic of the Hamamatsu model S10943-0258(X) SiPM array. Note that different cell tags are used in this thesis, as described earlier.

5.5.2 Gain Uniformity Tests for the 10, 2011 Article Units

The older electronic boards were not compatible with the new 10 pre-production units so a new electronic board had to be used, which had a different gain. The gain uniformity tests were done on the unit # 75. While comparing the most recent result with the result of measurements taken by the previous SiPM and electronic board, four major differences were found:

1. The pulse height was almost half of the prior results obtained with the 2010 SiPM unit, which confirms that the pre-amplifier gain for the new electronic board is half of the previous board's gain, as verified by Mr. Barbosa (JLab).
2. Instead of the 18 mV after-pulse that were seen with the previous electronic board

being used, there was a 10 mV pre-pulse detected, whose amplitude is almost half of the earlier after-pulse.

4. The pulse shape was different and it appeared to be saturated, while with the same set-up on the LED, the pulse was normal looking with the prior electronic boards and SiPM. After the “LED width” was decreased, the pulse became sharper one and did not saturate. However, it should be noted that when the LED width was decreased the pulse height was consequently decreased. This observation is consistent with the hypothesis that they were LED-induced and not caused by the new SiPM board combination. (The same LED was used for all the experiments.)

5.5.3 Results of the Gain Uniformity Tests for the 10, 2011 Article Units

All gain uniformity tests, including forward, backward, random, and cell-mapping scans, were done as described earlier, for all the 10 units. The pre-amplifier voltages were $-5 V$ and $5 V$. The bias voltage for each unit was different and set as it was reported by Hamamatsu. The bias voltage of each unit is shown in table at room temperature. 5.5.

Serial Number	75	76	77	78	79	80	81	82	84	85
Bias Voltage (V)	71.54	71.92	71.97	71.95	71.87	72.02	72.05	72.09	71.71	72.15

Table 5.5: Bias Voltages for the first article units.

For SiPMs 77 and 81, in order to increase the statistical power, each of the scans were done six times, excluding the cell-mapping scans which were done only one time. All

the results are shown in Appendix A. The result for unit 75 is shown in figure 5.12. The result of forward, random and backward scans are consistent with each other. The deviations from the average for these three tests are shown in figure 5.13. A subset of the rest of the 10 units, excluding unit 75, is shown in figure 5.14. All results are shown in appendix A. Figure 5.13 shows that the result from the all the three methods of scanning (forward, backward and random scans) are consistent. The deviations are deviations from the average of the pulse height from all of the cells, and the deviation for unit 75 is $\pm 10\%$

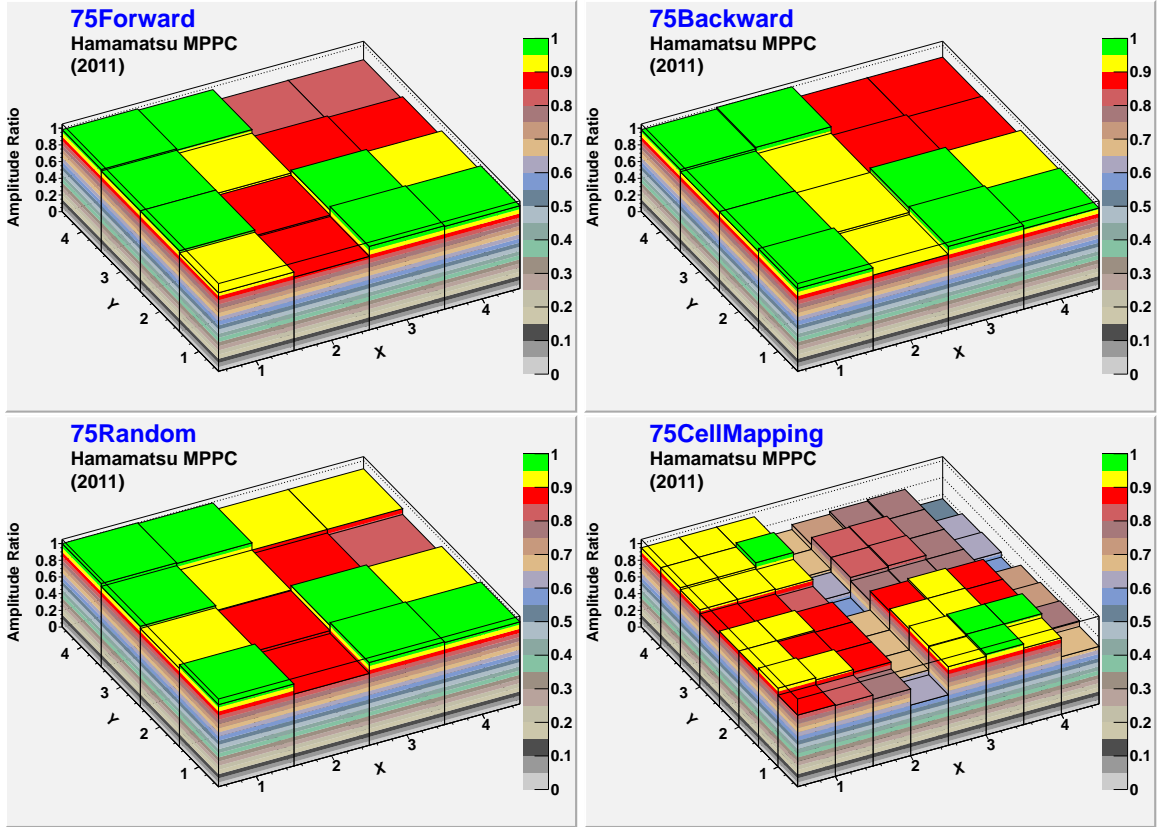


Figure 5.12: Unit 75, top left: forward scan, top right: backward scan, bottom left: random scan, bottom right: cell mapping (original in color)

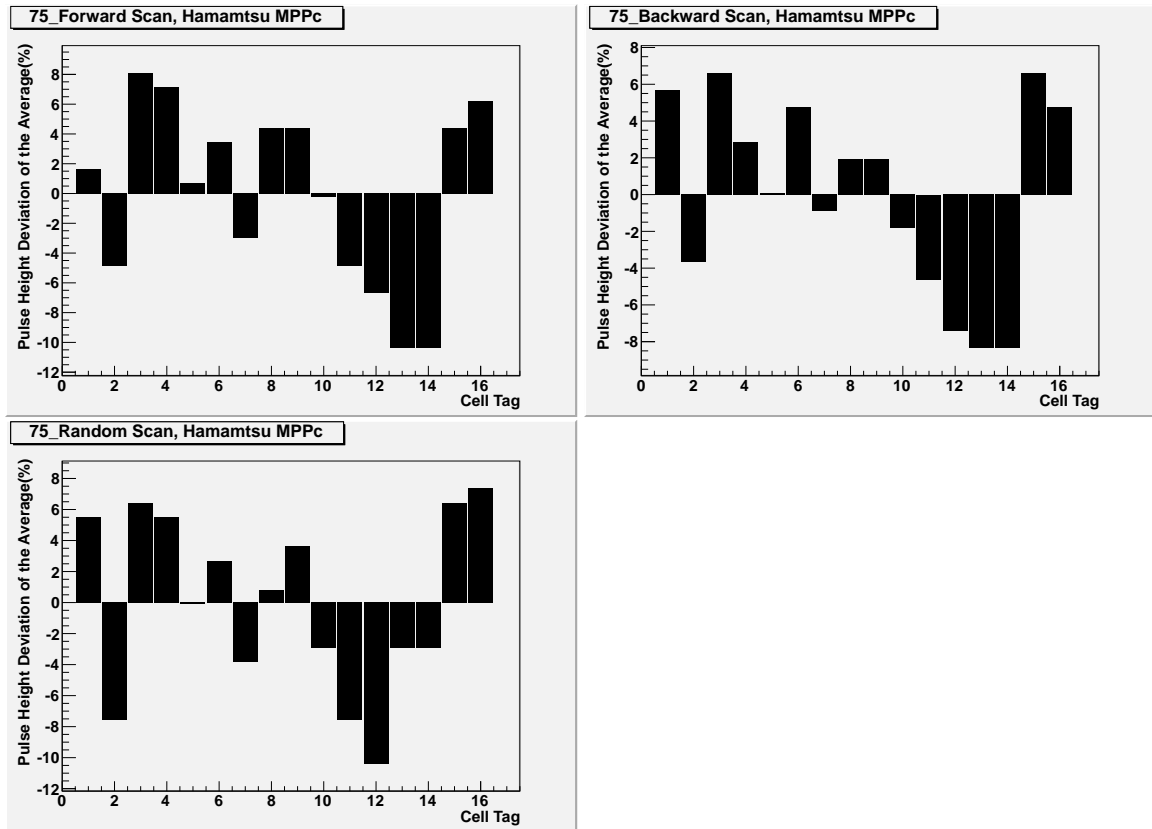


Figure 5.13: Unit 75, deviation from pulse height average, top left: forward scan, top right: backward scan, bottom left: random scan.

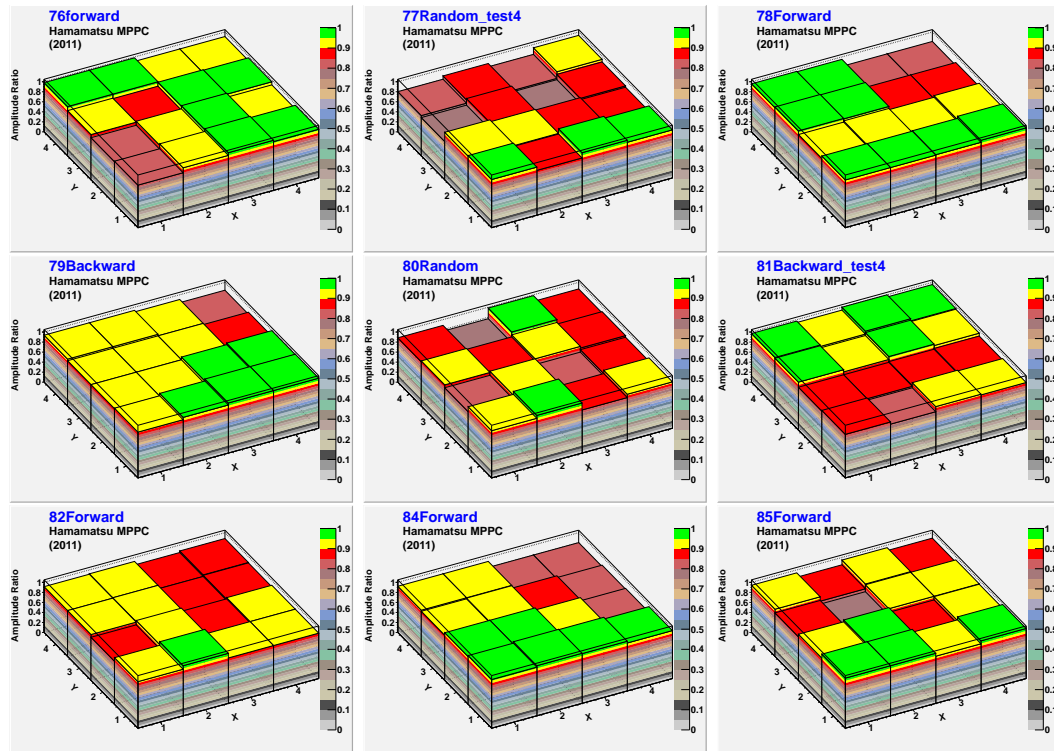


Figure 5.14: Gain Uniformity Scans for all the 10 article units excluding 75, top left: forward scan for unit 76, top middle: random scan for unit 77, top right: forward scan for unit 78, middle top: backward scan for unit 79, middle middle: random scan for unit 80, middle right: backward scan for unit 81, bottom left: forward scan for unit 82, bottom middle: forward scan for unit 84, bottom right: forward scan for unit 85. (original in color)

Chapter 6

Photon Detection Efficiency Extraction

6.1 PDE Device Construction

As mentioned earlier, the largest possible PDE is desired for the GlueX Experiment, in order to maximize energy and timing resolutions. This is particularly important for the detection of low-energy photons in the BCAL, which deposit a small amount of light in the fibers.

In order to obtain the absolute number of the photoelectrons produced in the SiPM, a setup was designed and constructed at the University of Regina as shown in figure 6.1.



Figure 6.1: Fiber Holder and Light Guide (FHLG) apparatus for the PDE measurements. For additional details the reader is directed to the text. Picture courtesy of Derek Gervais (U of R faculty of science).

For the PDE measurements, the SiPM is attached at one end of a fiber and a calibrated photodiode views the other end. If the fiber is completely symmetric, we expect to get the same amount of photons at each end of the fiber, and consequently the same amount of photons incident on the SiPM and the photodiode. At very low intensities the photodiode is replaced by a calibrated PMT, which is sensitive to such low amount of light, unlike the photodiode that has no amplification and therefore is suitable for only lighter incident flux intensities. The apparatus has to be symmetric for the photodiode and the PMT, as well. The design in figure 6.1 was the best possible design to achieve the above goal.

In figure 6.1, the fiber is rigidly held in place via a 300-*mm*-long fiber holder and within a 1-*mm* groove. The design for the fiber holder is shown in figure 6.2. So that the fiber would have exactly the same length as the fiber holder, SMA connectors

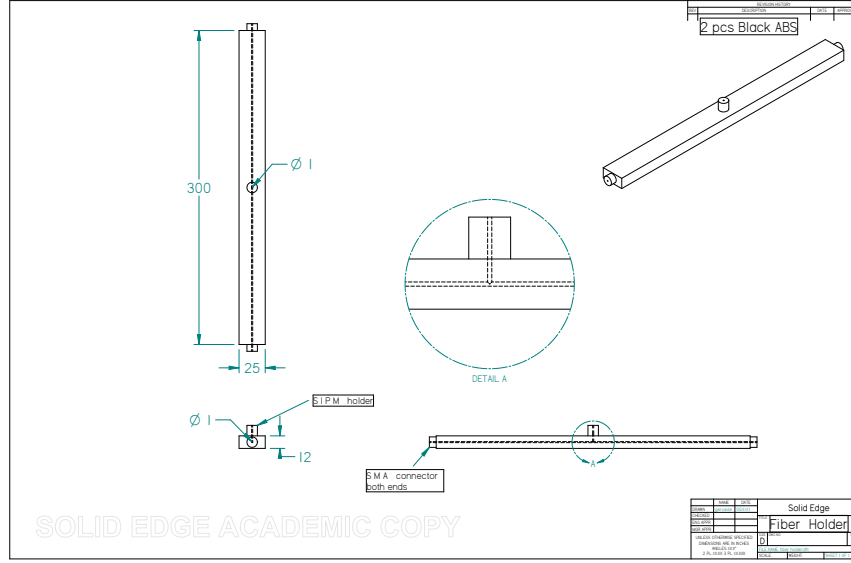


Figure 6.2: Details of the fiber holder for the PDE measurements (dimensions in millimeter). Picture courtesy of Derek Gervais. (original in color)

were temporarily fixed to the fiber holder by means of clips, and then were glued together while the fiber was in the fiber holder. The fiber was then trimmed and polished carefully by using the Clauss¹ Fiberoptic Polishing Kit.

The laser light is injected exactly at the centre of the fiber, because of the design of the fiber holder. A SMA barrel connector was installed at the centre of the fiber holder, to which the fiber transporting the light from the UV LED or laser could be affixed in a reproducible way.

The device also includes two aluminum tubes as shown in figure 6.1, which are originally designed as housings for PMTs. There is one light guide at each end of the fiber, as shown in figure 6.3. Both light guides have one tapered and narrow end with its flat area of the same dimension as the active area of the photodiode, which is a circle with diameter 8.99 mm. One of the light guides is coupled to either the

¹60 Round Hill Road, Fairfield, CT 06824, US.

photodiode or PMT, depending on the light intensity used. The other light guide is coupled to the SiPM. Two cylinders are used as inserts into the PMT housings in order to hold the SiPM and the photodiode/PMT sensors at the correct location, and firmly in contact against the light guides. The cylinders have custom designs to accommodate the different light sensors, but in all cases they align those sensors to the centre of the light guides.

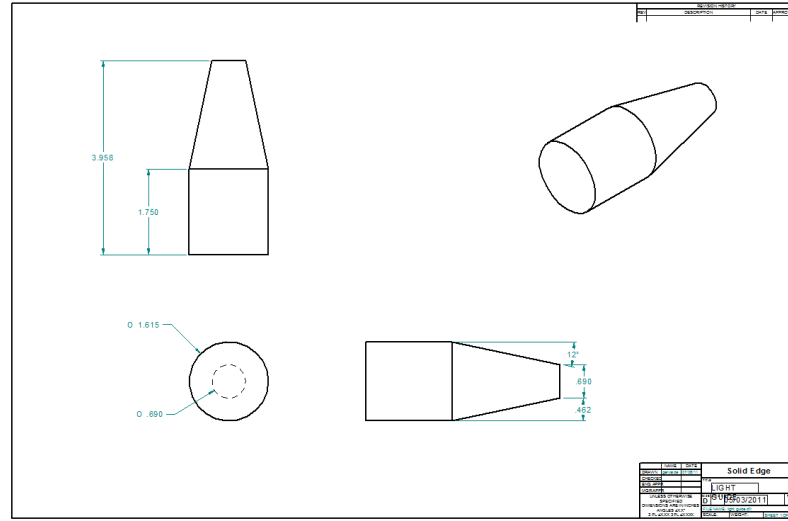


Figure 6.3: Light guide's dimensions in inches for the FHLG. Picture courtesy of Derek Gervais. (original in color)

The cylinder that holds the SiPM has a radius of 20.64 mm , and a length of 185.74 mm . The cylinder that holds the photodiode has a radius of 20.64 mm and a length of 187.32 mm . Detailed dimensions are given in figures 6.4 and 6.5.

Since the SiPM has an inactive area at its centre, as shown in figure 6.6, the cylinder that holds the SiPM was designed in a way that the fiber also can illuminate the SiPM off-centre with respect to the fiber's axis in order to illuminate an area of the SiPM with a fill factor more representative of the average for the unit.

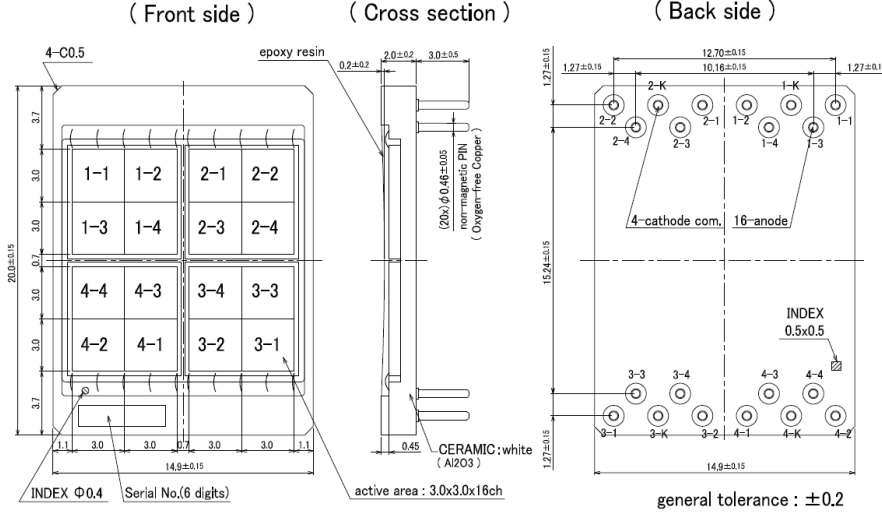


Figure 6.6: Hamamatsu SiPM showing the inactive area at its centre(left), and pinout connections on the back (right).

fill factor would be 0.809 for this setup, which is slightly less than the value of 0.8928 over the entire surface. In other words, if the whole area of the SiPM is illuminated ($12.7 \times 12.7 = 161.3 \text{ mm}^2$), the active illuminated area is ($12.0 \times 12.0 = 144.0 \text{ mm}^2$). Thus its fill factor will be $\frac{144.0 \text{ mm}^2}{161.3 \text{ mm}^2} = 0.8928$, without taking each pixel's inactive area into account. For the PDE measurements as shown in figure 6.7, the illuminated area is $\pi \times (9.00)^2 = 63.62 \text{ mm}^2$, and the illuminated active area is 51.51 mm^2 . Thus its fill factor, excluding each pixel's inactive area, will be 0.809.

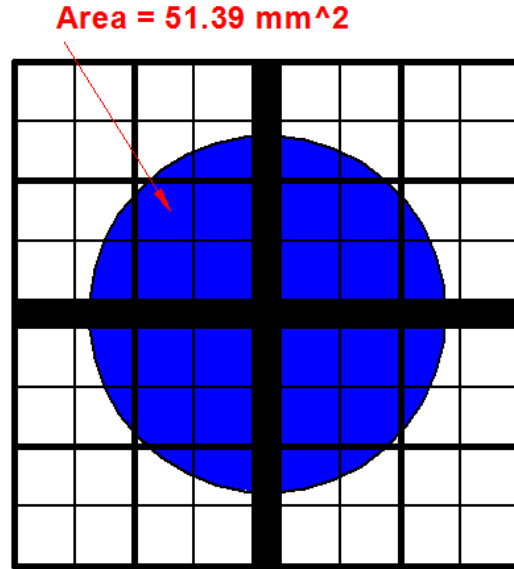


Figure 6.7: The active area illuminated by the laser for the PDE measurement is 51.39 mm^2 . (original in color)

6.2 PDE Measurements

The set-up for the PDE measurements contains the following devices:

- The FHLG.
- The dark box.
- Tektronix TDS 5104 Digital Phosphor Oscilloscope.
- 6487 KEITHLEY picoammeter/voltage source to provide the bias voltage and get the photodiode's current.
- Two power supplies to provide pre-amplifier voltages (DC Regulated Power Supply CSI3003 XIII, and Regulated DC Power Supply GP-1503).
- PDL 800-D pulsed diode laser or the UV LED.

- Delay lines.
- LeCroy² 2228A TDC.
- LeCroy 2249A 12 CHAN “Analog to Digital Converter” (ADC). The basic function of an ADC is to generate a number which is proportional to an analog voltage given to it [19]. It actually converts the information contained in the analog pulse into an equivalent digital form.
- HYTEC³ 1331/TURBO P.C. CAMAC interface.
- Computer to get the ADC result.
- CAEN⁴ 3 Fold Logic Unit.
- Model 705 octal discriminator.
- S2281 Hamamatsu photodiode.
- Hamamatsu model R329-02 calibrated PMT.

Depending on whether the laser or the LED were used, different electronic circuits were used as shown in figures 6.8 and 6.9.

Figures 6.10 and 6.11 show the FHLG in the dark box, the laser, the set-up to get the photodiode current, the resulting SiPM pulse, and the units that provide the pre-amplifier voltages. In order to obtain the ADC spectrum for the SiPM, the SiPM was disconnected from the oscilloscope and then was connected to the ADC and CAMAC system.

²700 Chestnut Ridge Road, Chestnut Ridge, NY, 10977-6499 (<http://www.lecroy.com/>)

³5 Cradock Road, Reading, RG2 0JT, United Kingdom (<http://www.hytec-electronics.co.uk/>)

⁴CAEN Technologies, Inc., 1140 Bay Street, Suite 2C, Staten Island, NY 10305 - USA (<http://www.caen.it/>)

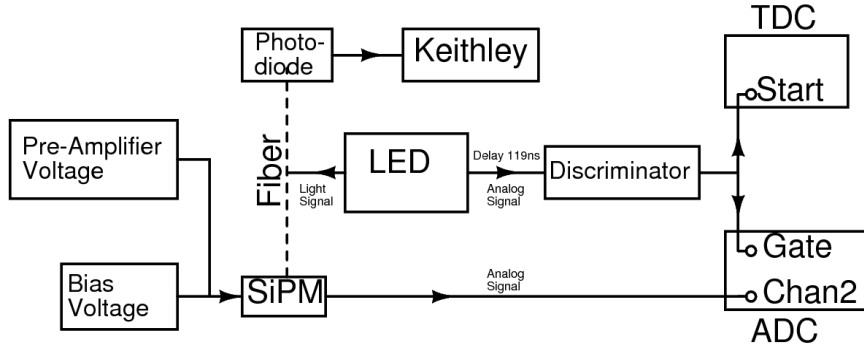


Figure 6.8: The PDE electronic circuits when the UV LED is being used.

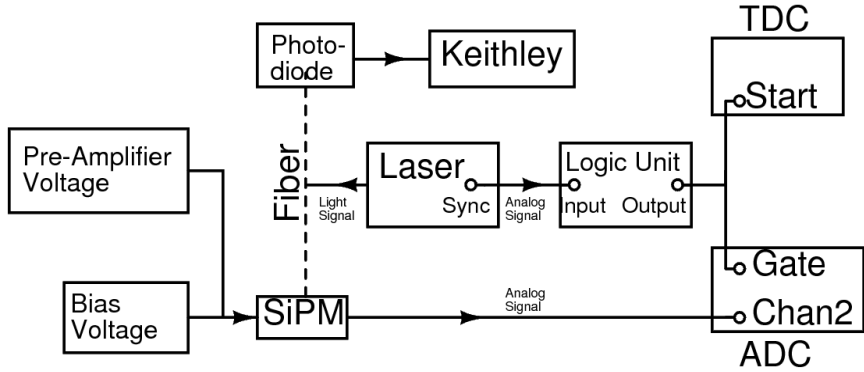


Figure 6.9: The PDE electronic circuits when the laser is being used.

6.2.1 Symmetry of the PDE Device

After the device was built, cross checks were carried out before proceeding with the measurement of the PDE to assure the accuracy and reproducibility of the PDE measurements. The first step was to ensure that the FHLG gives symmetric results. The next steps were to understand how the laser functions.

As described, the FHLG was designed to be as symmetric as possible as far as light distribution to each end is concerned. To ensure the symmetry, the SiPM was held at one end of the FHLG – side 1 – by means of the SiPM holder without any photodetector at side 2. The laser’s intensity was changed from 1.5 to 7, and the



Figure 6.10: A picture of the FHLG in the dark box. SiPM is held at side 1 and the photodiode is held at side 2. (original in color)

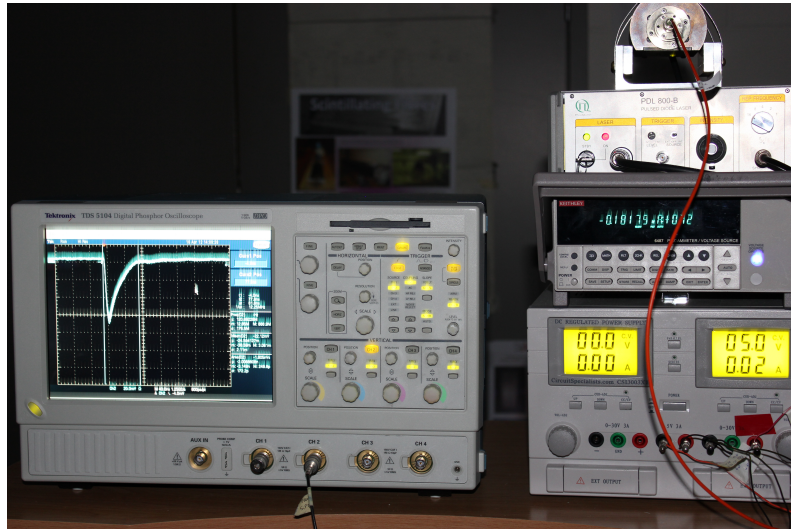


Figure 6.11: A picture of the oscilloscope, laser and the power supplies for the pre-amplifier and the bias voltages. (original in color)

output signals were recorded. The same test was done with the SiPM at side 2 without photodetectors at side 1. The results of both tests were the same and are shown in figure 6.12. The vertical axis is the pulse height of the SiPM seen on the oscilloscope, and the horizontal axis is the intensity set on the laser.

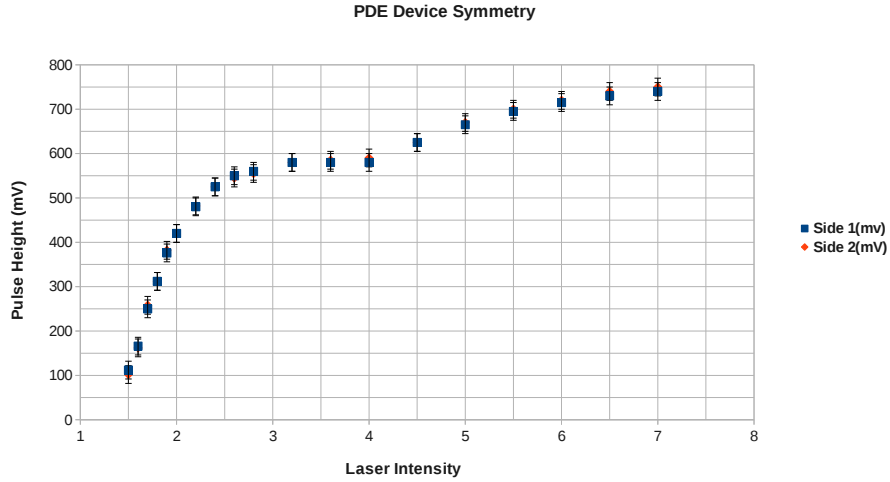


Figure 6.12: A test to find how symmetric the FHLG was. The result for both sides of the FHLG are the same (arbitrary units). (original in color)

6.2.2 SiPM vs. PMT Using an External Trigger

The first set of measurements was taken with the laser being triggered externally at 44.9 kHz . The calibrated PMT and the Hamamatsu S10943-0258(X) SiPM array were employed. The intensity of the laser dial was varied from 1.45 to 2. Figures 6.13 and 6.14 show the results. The vertical axis of the plot is calculated as shown in equation (6.1), which shows the number of photoelectrons (NPe) and the x-axis is the value of $(ADC - ADC_{dark})$.

$$NPe = (ADC - ADC_{dark})^2 / (RMS^2 - RMS_{dark}^2) \quad (6.1)$$

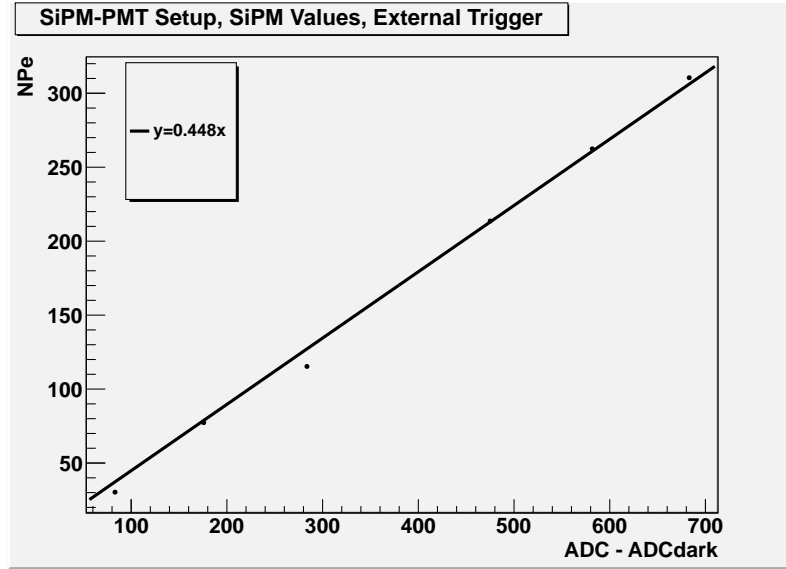


Figure 6.13: SiPM NPe values with an external trigger being used.

In figure 6.13, the NPe value of the SiPM is plotted versus its values of $(ADC - ADC_{dark})$. The linear fit is relatively good since both the axes are the values for a same device (SiPM), and both of the values are affected in a similar way.

In figure 6.14, however, since the vertical axis is the NPe value of the SiPM and the horizontal axis is the values of the PMT, and since the PMT and the SiPM react differently to the noise, in figure 6.14 the values are not a good linear fit. This is most likely due to the fact that when the laser was triggered externally, particularly at low intensity levels, the signal to noise ratio was poor. It should be noted that the PMT is designed to perform at low light intensities, and the relative SiPM noise at low intensities is not negligible. Thus, it is concluded that “PMT vs. SiPM method” was not the best method for the PDE tests. Thus more tests were not done using this method.

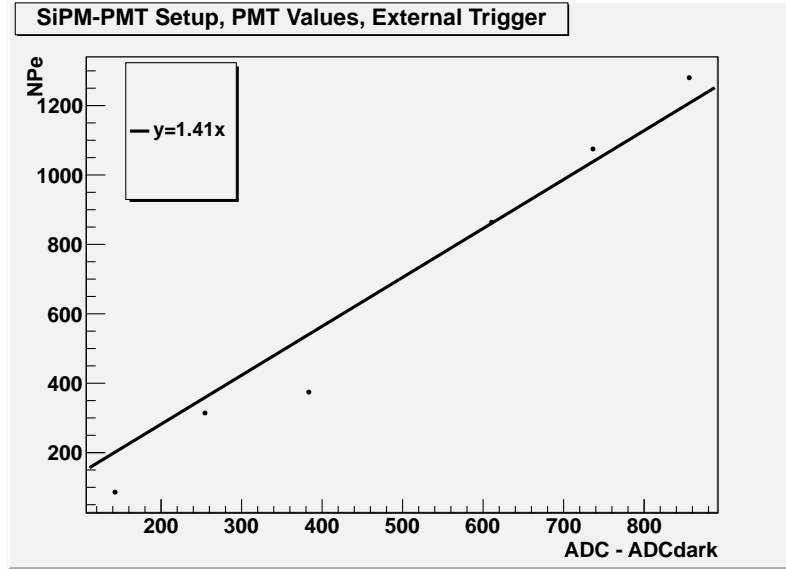


Figure 6.14: PMT values with an external trigger being used.

6.2.3 Photodiode Current Scan Over the Laser Frequency

The next step was to understand the photodiode's performance. So the photodiode was positioned in the setup instead of the SiPM, and the PMT was turned off. The laser external frequency was changed from 50 kHz to 2 MHz , and the photodiode current was read out with a Keithley picoammeter. It was noticed that when the external frequency was increased, at low intensities, the current out of the photodiode was about the same as the dark current. Specifically, at the frequency of 2 MHz , the current out of the photodiode was the dark current for all intensities from 1.45 to 2 (arbitrary units).

To assure that this was a result of the laser's behavior and not the photodiode's or the picoammeter's, the SiPM was positioned instead of the photodiode and the same result was obtained. The output signals of the SiPM were zero at 2 MHz for intensities up to level 2.

In order to investigate whether there was a problem with the external trigger, the integral trigger of the laser was tested and the SiPM signal output showed up at intensity level of 2.2, so this behavior is not the gate generator's behavior, which triggers the laser externally.

It should be noted that the laser's intensity level is not linear. Scans were carried out employing either the SiPM or the photodiode in the FHLG, and the resulting behavior is far from linear over the entire scanned range. The results are shown in figures 6.15 and 6.16. Where necessary, extracted measurements were corrected to account for this behaviour.

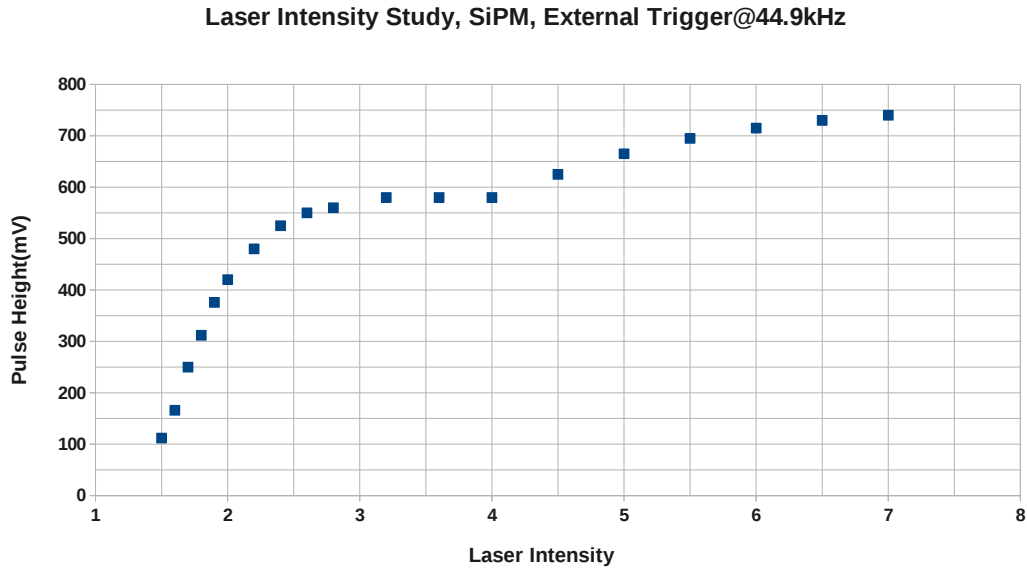


Figure 6.15: Laser intensity investigation with the SiPM being used. The laser was triggered at 44.9 kHz , externally (arbitrary units).

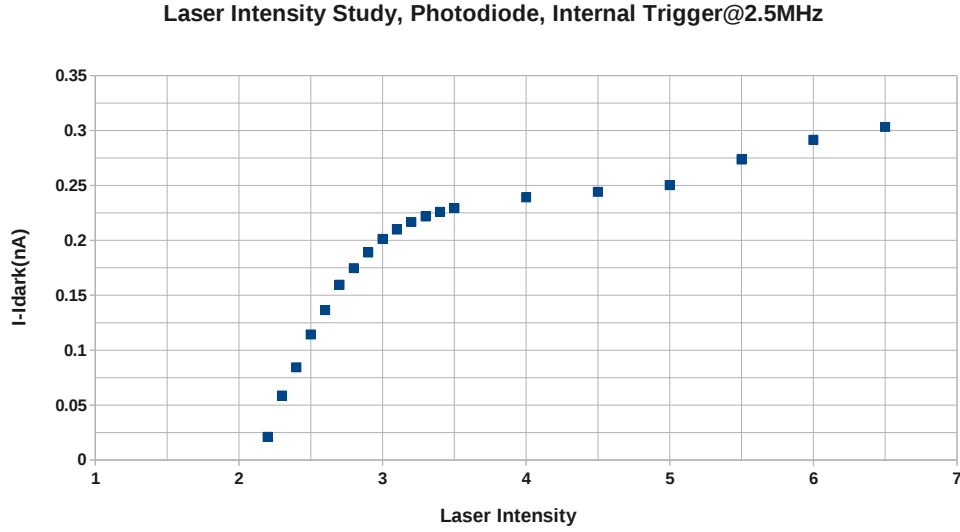


Figure 6.16: Laser intensity investigation with the Hamamatsu photodiode utilized. Laser was triggered at 2.5 MHz , internally (arbitrary units).

6.2.4 Frequency and Intensity Scan, Photodiode vs. PMT, Laser Triggered Externally

With the symmetry of the FHLG having been verified by measurement, the investigation could proceed to extract the PMT and the photodiode calibrations. So for this test, the photodiode and the PMT were held by the FHLG, the laser was triggered externally and the frequency was changed from 39 kHz to around 500 kHz , while the intensity level was also changed from 1.5 to 2.

The PMT voltage were set at 1450 V . There were no pulses detected by the PMT for the intensity level of 1.45, so the scan over the intensity level was started from 1.5 and the outputs of the PMT and the photodiode were recorded off the oscilloscope.

To completely analyze the system several graphs were plotted. One of the graphs was to study the photodiode. The graph shows I_{corr} of the photodiode versus the frequency of the laser. I_{corr} was calculated as shown in equation (6.2).

$$I_{corr} = I_i(ADC - ADC_{dark})/(ADC_i - ADC_{ped}) \quad (6.2)$$

Where I_{corr} is the corrected current for the photodiode, and I_i is the current read from the picoammeter for each individual intensity. The plot is shown in figure 6.17. Fits are programmed to pass through the origin of both axes. There are seven lines shown in the plot with different colors, with each color being for a different intensity level of the laser. Figure 6.17 shows the relationship between the current of the photodiode and the frequency of the laser. For all intensities the relationship is linear, however, for different intensities the slope of the linearity is different. When the intensity is increased, at higher frequencies the data points drop down from the linear fit, which might be due to invisible saturation of the PMT.

6.2.5 ADC Background

In order to understand the ADC background, two sets of tests were done on two different days and times. For all the sets the SiPM was installed in the FHLG. The SiPM was connected to the ADC, the laser intensity level was set at zero, the pre-amplifier voltages were +2.17 V and -5.00 V, the bias voltage was off for one set and was 70.79 V for the other one. The first test was on the integrated charge due to “electronic noise” in pre-amplifier and ADC. The second set of measurements represents the “true” dark noise of the SiPM and it is dominated by one or two photoelectrons. Each test was repeated five times in each day at different times, in order

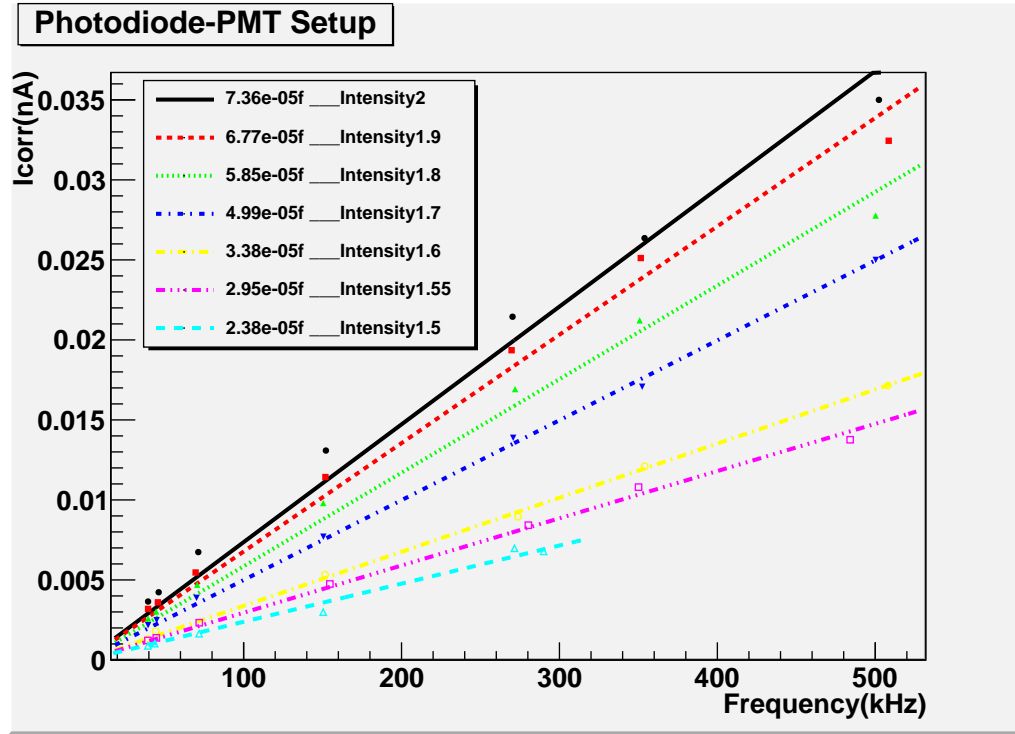


Figure 6.17: Photodiode and PMT response to the external frequency of the trigger for seven different intensity levels of the laser. (original in color)

to find how consistent the results are with different conditions such as temperature, changes in voltages and noises, and etc. Figure 6.18 shows the ADC values versus the run numbers. The runs were in different times in a day and the tests were carried out on two different days. The data over time were consistent, which was true also for the second set (bias voltage was on). Figure 6.18 shows that the results on different days are consistent with each other and the deviation is small.

For the third set of tests, the SiPM output signal cable was disconnected from the ADC module and a $50\ \Omega$ terminator was connected, instead. As shown in figure 6.21, the pedestal is not exactly zero and it should be incorporated to the PDE calculation. Figure 6.19 shows the dark current of the SiPM that also must be considered for the PDE calculation. Figure 6.20 shows that besides the SiPM dark current, the pre-

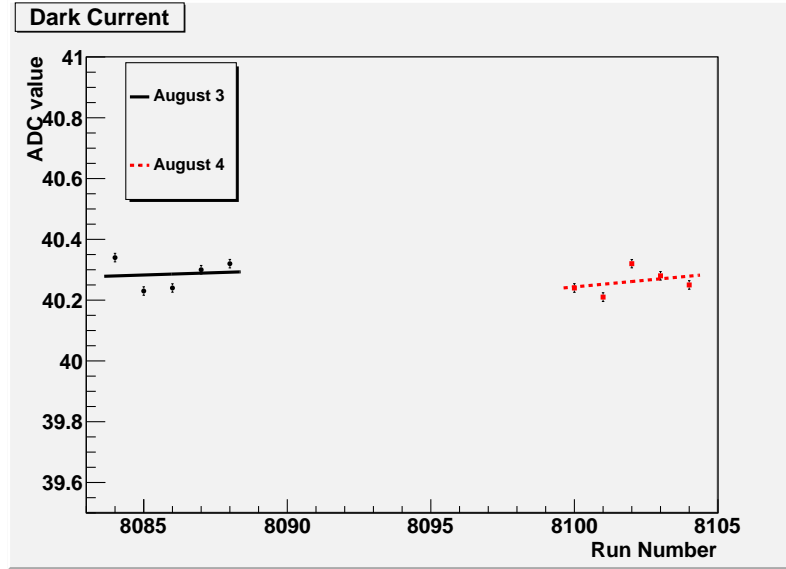


Figure 6.18: Observation for the dark current at different times. The data over time were consistent, The SiPM's pre-amplifier voltages were set at +2.17 V and -5.00 V, respectively, bias voltage was at 70.79 V, and the laser intensity was set at zero. (original in color)

amplifier voltage contributes to noise in the system. The higher mean in figure 6.19, compared to that of figure 6.20 (34.65 vs 22.18), represents the contribution of the SiPM and constitutes the “dark” contribution to the number of the photoelectrons generated in the SiPM. Finally, figure 6.21 displays the “true” ADC pedestal.

6.3 Intensity Scan, Photodiode vs. SiPM, Laser Triggered Internally

For this test, the frequency was set at 2.5 *MHz* and the intensity was changed from level of 2.2 to the highest possible level. Note that several factors determine the highest intensity level. First of all, there was consideration to assure that the

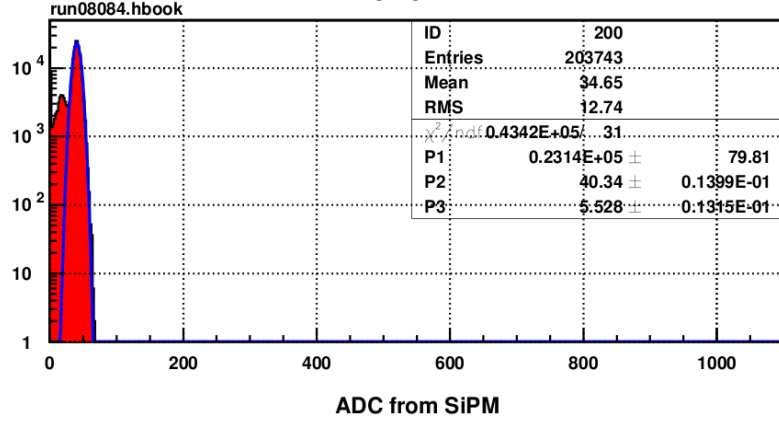


Figure 6.19: The SiPM was connected to the ADC, the pre-amplifier voltages were set at 2.17 V and -5.00 V, the bias voltage was set at 70.79 V, and the laser was triggered internally at 2.5 MHz with zero intensity. The figure represents the “true” dark noise of the SiPM and it is dominated by one or two photoelectrons. The laser was on, in order to take into account the noise produced when the laser was on, as well as to generate a gate for the TDC. (original in color)

pulse out of the SiPM was not saturated. Secondly, the number of the produced photoelectrons must be within the linear dynamic range of the ADC.

For this test, the most important graphs are shown in figures 6.22 and 6.23. Figure 6.22 shows the output current of the photodiode versus the $(ADC - ADC_{dark})$, the line is fitted in a way that it passes through the origin of the frame. In figure 6.23 the vertical axis of the plot is calculated as shown in equation 6.1 which shows the number of photoelectrons at the SiPM, and the x-axis is the value of $(ADC - ADC_{dark})$.

6.4 PDE Extraction for the First Article Units

The PDE extraction for the 10 units was done using both the UV LED and the laser, using different intensities (intensity scan). For both of the scans, at one side of the

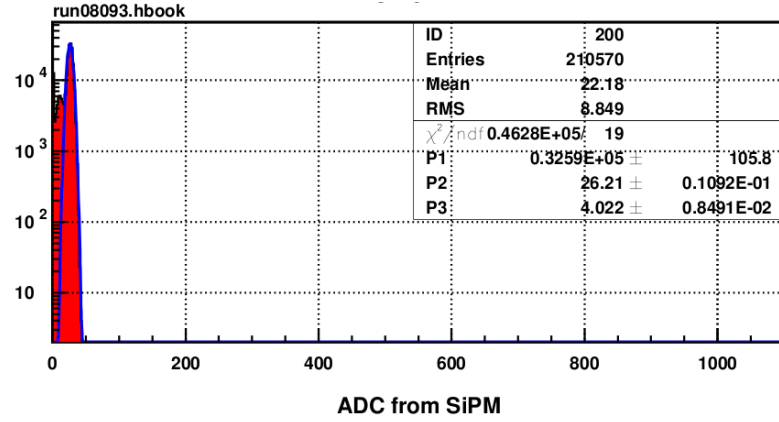


Figure 6.20: The SiPM was connected to the ADC, the pre-amplifier voltages were set at 2.17 V and -5.00 V, bias voltage was off, the laser was triggered internally at 2.5 MHz. The picture is the integrated charge due to “electronic noise” in pre-amplifier and ADC. (original in color)

FHLG the photodiode was used, while at the other end the SiPM. Depending on whether the scans were done by the LED or by the laser, at the middle of the FHLG, either the LED fiber or the laser fiber were connected.

The intensity dial of the LED, which was used for the scans, was not calibrated. So, we first calibrated the dial by measuring the current of the photodiode and the pulse height of the SiPM on the oscilloscope. Eight specific points were chosen and marked on the dial. Later on, by extracting PDE values for each of the intensity values chosen, it was found that the first point on the dial had such a small intensity that it could not be counted as a reliable result. Thus, the first intensity setting was deleted from the data to make the plots. The second point on the dial, as well, had a small intensity, but because its extracted PDE was close to other values it was not excluded from the graphs. In the cases that its PDE value had a big difference from the other PDE values, it was excluded from the graphs.

For all of the 10 units the graphs of LED scans are provided in figure 6.24, and the

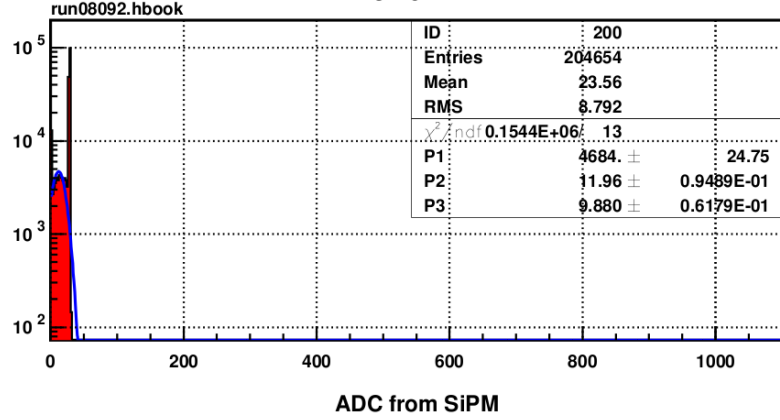


Figure 6.21: The SiPM was disconnected from the ADC and the $50\ \Omega$ terminator was connected, instead. The figure represents the “true” ADC pedestal. The blue fit is a Gaussian fit, P1 and P2 are of interest. P1 is the mean value for the Gaussian fit and P2 is the width of the Gaussian fit. (original in color)

relationship of NPe and the $(ADC - ADC_{dark})$ is linear. The fits in the graphs are forced to pass through the origin. So the relationship is forced to be as follows:

$$NPe = a \cdot (ADC - ADC_{dark}) \quad (6.3)$$

The average result of all the units is as follows:

$$NPe = (1.18 \pm 0.05) \cdot (ADC - ADC_{dark}) \quad (6.4)$$

The other graph which is useful is the photodiode current versus the $(ADC - ADC_{dark})$ as shown in figure 6.25. The error bars are included in the graphs at figures 6.24 and 6.25, but they are relatively small and cannot be seen clearly in the scale used in the graphs. The average result of all the units is as follows:

$$(I - I_{dark}) = (0.117 \pm 0.013) \cdot (ADC - ADC_{dark}) \quad (6.5)$$

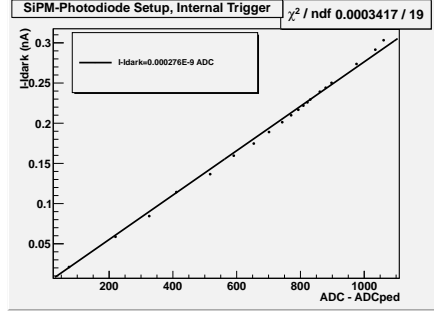


Figure 6.22: First set of PDE measurements showing the photodiode current versus the pedestal-subtracted ADC value. The laser was triggered internally at 2.5 MHz .

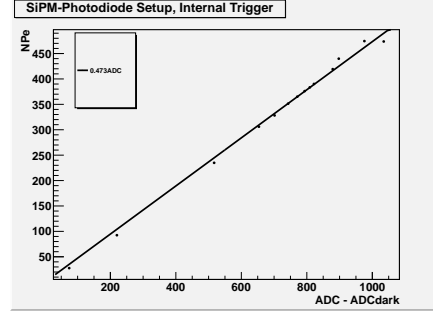


Figure 6.23: First set of PDE measurements showing NPe versus the pedestal-subtracted ADC value. The laser triggered internally at 2.5 MHz .

6.4.1 Incident Photon Determination

The number of incident photons was calculated using the photodiode and the following formula:

$$NPho = \frac{I - I_{dark}}{E_{(\lambda=460nm)} \cdot S_{(\lambda=460nm)} \cdot f_{LED}} \quad (6.6)$$

Where $NPho$ is number of incident photons, I is the current of the photodiode, and I_{dark} is the current of the photodiode when the intensity of the LED or the laser is zero. $E_{(\lambda=460nm)}$ is the energy of one photon with a wavelength of $\lambda = 460nm$, which is given through $E = \frac{hc}{\lambda}$, where h is the plank constant, c is the speed of light. $S_{(\lambda=460nm)}$ is the sensitivity of the photodiode, which according to Hamamatsu specific sheet for the calibrated photodiode is 228 mA/W for $\lambda = 460nm$. f_{LED} is the frequency of the LED as read from the oscilloscope.

Figure 6.27 shows the spectral sensitivity, S , and the QE of the Hamamatsu SS2281 photodiode as a function of wavelength. The spectral sensitivity needs to be convoluted with the fiber emission spectrum, in order to suitable modify the latter. The

middle plot shows a rebinned spectral sensitivity (SW, to match the binning of the fiber spectrum) on the left vertical axis, with both the original and rescaled (SW2) spectra on the right vertical axis, in arbitrary units of relative intensity. The bottom plot shows the spectrum and SW2 on a similar scale, to emphasize the change in the shape of the distribution, after the spectral sensitivity has been convoluted.

In figure 6.26, the green-brown panel shows the relative spectral intensity without and with the spectral sensitivity convolution. The top panel displays the relative spectral intensity of a Kuraray SCSF-78MJ blue-green fiber, with a 373 nm UV LED stimulating it at two different distances from the readout end, which is plugged into a spectrophotometer⁵.

Wavelength spectra with the LED positioned at 10 cm, and 30 cm are shown in figure 6.26 and in the bottom panel only the 10 cm and 30 cm spectra with their fits using double Moyal functions are shown. The Moyal distribution is often used as a good approximation to the Landau distribution [36]. Single Moyal function fits have four parameters including an amplitude (a), a characteristic wavelength and width (given by μ and σ) and a background term (b). The Kuraray SCSF-78MJ fiber spectra require a sum of two Moyal functions plus a flat background. In other words, the double Moyal fits introduce three additional parameters: they are characterized by two wavelengths (μ_1 and μ_2) and corresponding widths (σ_1 and σ_2), in addition to two amplitudes (a_1 and a_2) and a flat background (b), as follows:

$$f(x, a_1, \mu_1, \sigma_1, a_2, \mu_2, \sigma_2, b) = a_1 \cdot \exp \left(-\frac{1}{2} \left(\frac{(x - \mu_1)}{\sigma_1} + e^{-(x - \mu_1)/\sigma_1} \right) \right) + a_2 \cdot \exp \left(-\frac{1}{2} \left(\frac{(x - \mu_2)}{\sigma_2} + e^{-(x - \mu_2)/\sigma_2} \right) \right) + b \quad (6.7)$$

⁵Ocean Optics Inc., Dunedin, FL, USA (www.oceanoptics.com)

The idea behind selecting only the 10 *cm* and 30 *cm* measurements was dictated from the length of the fiber used in the setup, which was 15 *cm* from the light source input to each side of FHLG. No such measurement had been taken, so it was decided to effectively average the 10 *cm* and 30 *cm* data, as described below. Specifically, both spectra were fit with a double Moyal function, with the parameters shown in the table below. Subsequently, in order to determine the median of each spectrum, the spectra were first smoothed and then their running integrals were computed, as shown in the middle and bottom panels, respectively. Finally, the median values are shown on the top plot, at 459 *nm* and 462 *nm* for the 10 *cm* and 30 *cm* spectra, respectively. It was decided to use $460.5 \pm 1.5 \text{ nm} \simeq 460 \text{ nm}$ in the calculations of the photodiode current.

	a_1	μ_1	σ_1	a_2	μ_2	σ_2	b
30- cm fit	0.20317 ± 0.0222	434.61 ± 0.609	9.5956 ± 0.509	0.44994 ± 0.0203	453.13 ± 0.771	19.356 ± 0.23	-0.00060076 ± 0.000351
10- cm fit	0.62659 ± 0.00513	439.78 ± 0.379	15.002 ± 2.11	0.11315 ± 0.00963	479.78 ± 1.31	19.65 ± 0.353	0.00083298 ± 0.000385

Table 6.1: Parameters of the double Moyal function, for the 10-cm and 30-cm fits.

6.4.2 PDE Extraction Methods

Three methods were developed and employed to extract the PDE values, and an average value was found for each SiPM Unit. The results are shown in table 6.2.

Method 1 is the most accurate method and uses the RMS and ADC values of the digital signals:

$$NPe = \frac{(ADC - ADC_{dark})^2}{RMS^2 - RMS_{dark}^2}. \quad (6.8)$$

# SiPM	Method 1	Method 2	Method 3
75	13.05 ± 0.86	23.19 ± 5.82	17.74 ± 1.61
76	17.23 ± 0.74	25.69 ± 1.78	21.64 ± 1.05
77	19.23 ± 1.04	18.90 ± 1.18	25.16 ± 1.17
78	16.29 ± 0.93	18.78 ± 2.01	20.08 ± 1.20
79	18.43 ± 2.67	22.31 ± 1.30	24.31 ± 2.55
80	16.65 ± 0.86	20.55 ± 1.79	21.51 ± 1.24
81	17.51 ± 0.89	21.84 ± 1.45	22.30 ± 1.25
82	18.10 ± 0.92	24.64 ± 0.96	24.83 ± 1.11
84	17.14 ± 1.00	23.57 ± 1.57	24.45 ± 1.31
85	17.58 ± 1.19	21.98 ± 2.68	22.93 ± 1.44

Table 6.2: PDE values for the 10 units using the LED. For each SiPM unit, the average PDE of the intensity scan is reported, and the reported uncertainty is the standard deviation of the PDE values for each unit with different intensities. These values are raw values and no corrections have been applied to account for the fill factor.

Method 2 uses the pulse characteristics to find the number of photoelectrons:

$$NPe = \frac{(A)}{(50\Omega) \cdot e \cdot G}. \quad (6.9)$$

Where A is the pulse area read from the oscilloscope as shown in figure 6.28. The oscilloscope gives the pulse height and the area of the pulse. e is charge of an electron, 50Ω is the resistance used at the oscilloscope as a terminator, and G is the total gain of the SiPM and its electronic board.

Method 3 uses the ADC measurement as follows:

$$NPe = \frac{(ADC - ADC_{dark}) \cdot (q)}{e \cdot G}. \quad (6.10)$$

Where q is the electric charge for one ADC spectrum unit, which for the ADC used in the test is 0.25 pC , e is the charge of an electron, G is the total gain of the SiPM and its electronic board.

The number of photons and number of photoelectrons from all three methods are plotted on the left and right vertical axes in figure 6.29, respectively. The PDE, calculated from the ratio N_{pe}/N_{pho} is plotted on the bottom plot, for all three methods. The zone in the box has been determined to be unstable based on the behavior of the LED at such low intensity values. Beyond that region, all three PDEs are approximately constant, as is expected. The difference in magnitudes is attributed by the method of charge estimation but particularly by the differing errors in those methods having the RMS in the denominator.

6.4.3 Laser Intensity Scan

The results for different intensities of the LED were not perfectly consistent with each other, thus for a more thorough investigation for three of the SiPM units the laser intensity scan was done as well, in addition to the LED intensity scan. The results were much more consistent over different laser intensities.

The PDE for all the intensities was extracted by using the three different methods above, and an average value were found for each SiPM Unit. The results are shown in table 6.3.

# SiPM	Method 1	Method 2	Method 3
76	19.64 ± 0.48	22.18 ± 0.91	21.64 ± 1.05
78	16.29 ± 0.93	18.78 ± 2.01	20.08 ± 1.20
85	17.58 ± 1.19	21.98 ± 2.68	22.93 ± 1.44

Table 6.3: PDE values for the 3 of the units by using the laser. For each SiPM unit the average PDE of the intensity scan is reported, the reported uncertainty is the standard deviation of the PDE values for each unit with different intensities. These values are raw values and no corrections have been made for effective fill factor.

Figure 6.30 shows the PDE values using the three methods, and the values are corrected for the inactive area. These initial results are quite promising, and in agreement with those measured at USM Chile [37], while consistent to the ones measured at JLab [37].

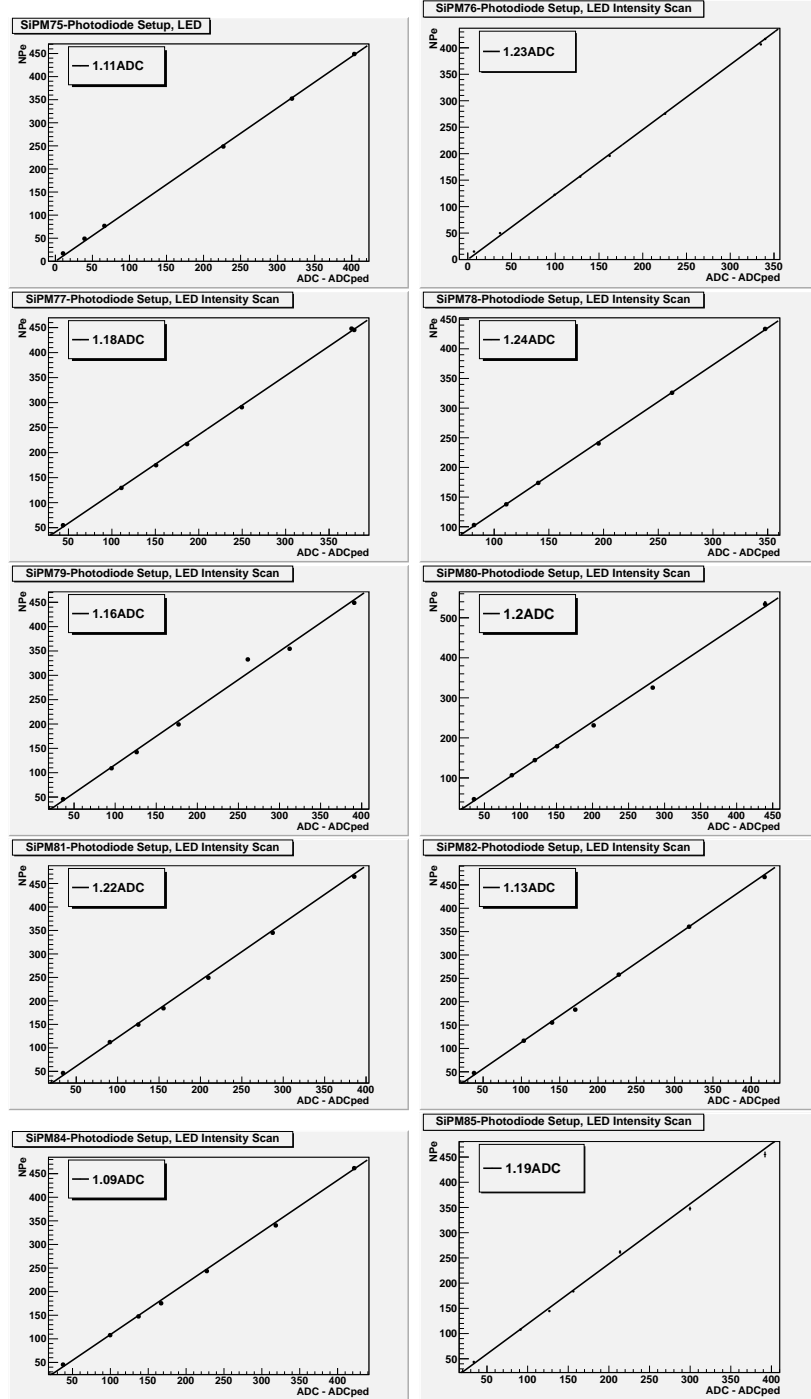


Figure 6.24: For the PDE extraction intensity scans were done for all the SiPM units using the LED; the vertical axis is the number of the photoelectrons using formula 6.1, and the horizontal axis shows the $ADC - ADC_{dark}$.

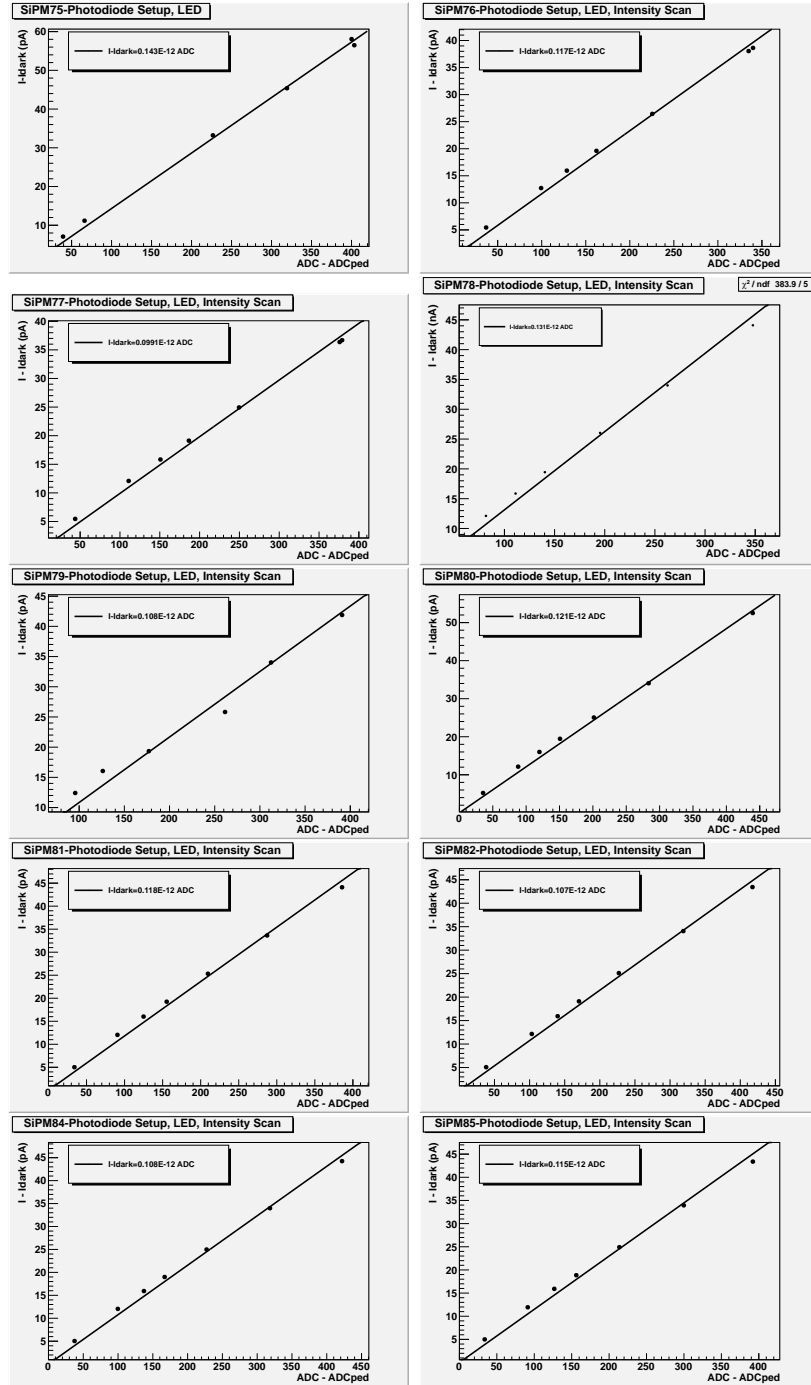


Figure 6.25: For the PDE extraction intensity scans were done for all the SiPM units using the LED; the vertical axis is the current of photodiode ($I - I_{dark}$) and the horizontal axis is the $ADC - ADC_{dark}$.

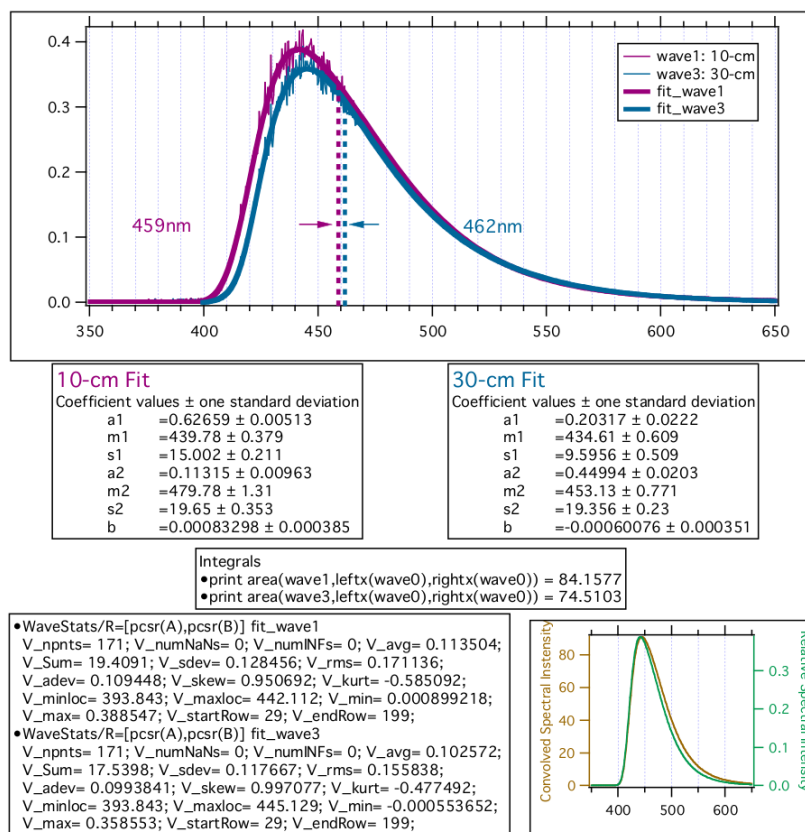


Figure 6.26: The top panel displays the relative spectral intensity of a Kuraray SCSF-78MJ blue-green fiber, with a 373 nm UV LED stimulating it at two different distances from the readout end. The green-brown panel shows the relative spectral intensity without and with the spectral sensitivity convolution, respectively. (original in color)

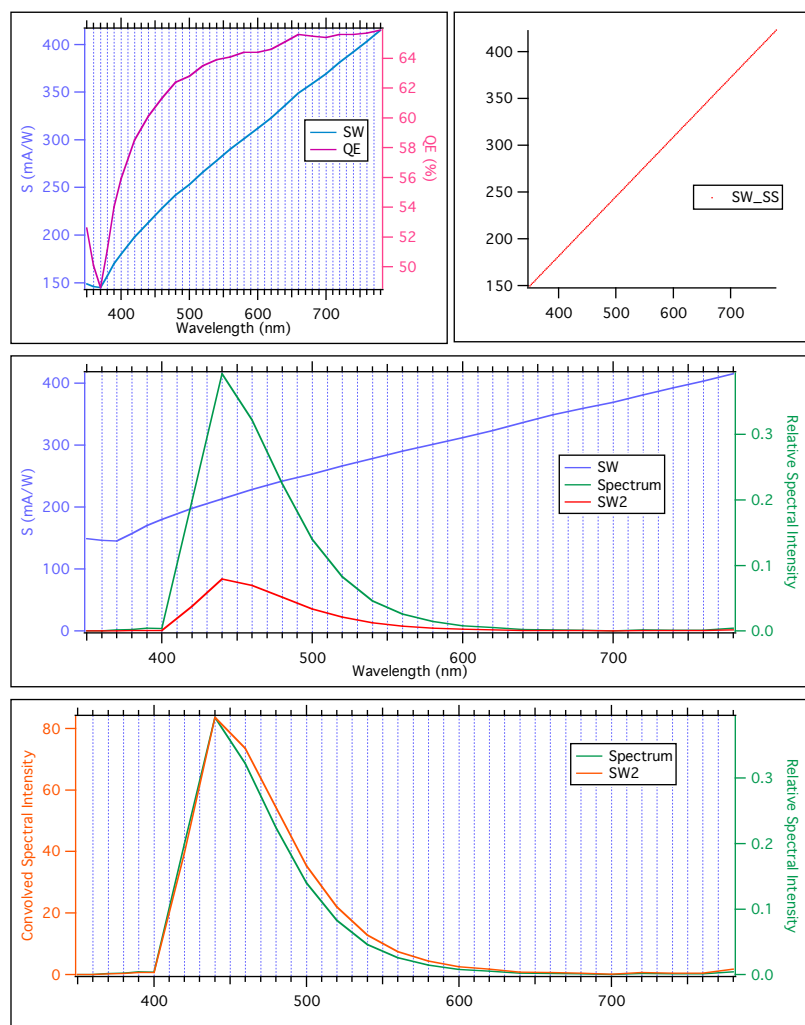


Figure 6.27: Top: S and QE of the Hamamatsu photodiode as a function of wavelength. Middle: a rebinned spectrum sensitivity. Bottom: convolved spectral intensity as a function of wavelength. (original in color)

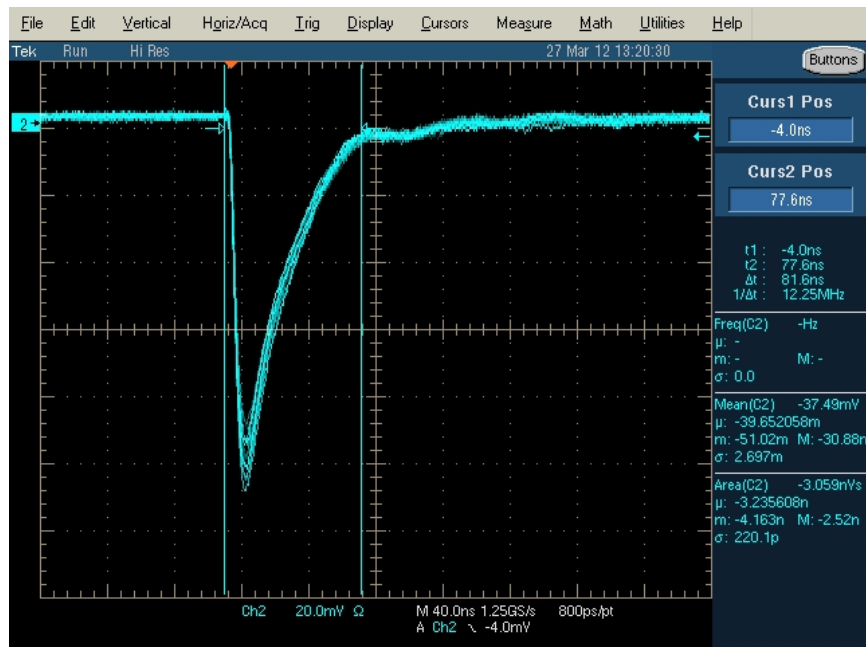


Figure 6.28: The pulse shape of one of the SiPM units, using the laser. The oscilloscope is able to provide the area of the pulse. (original in color)

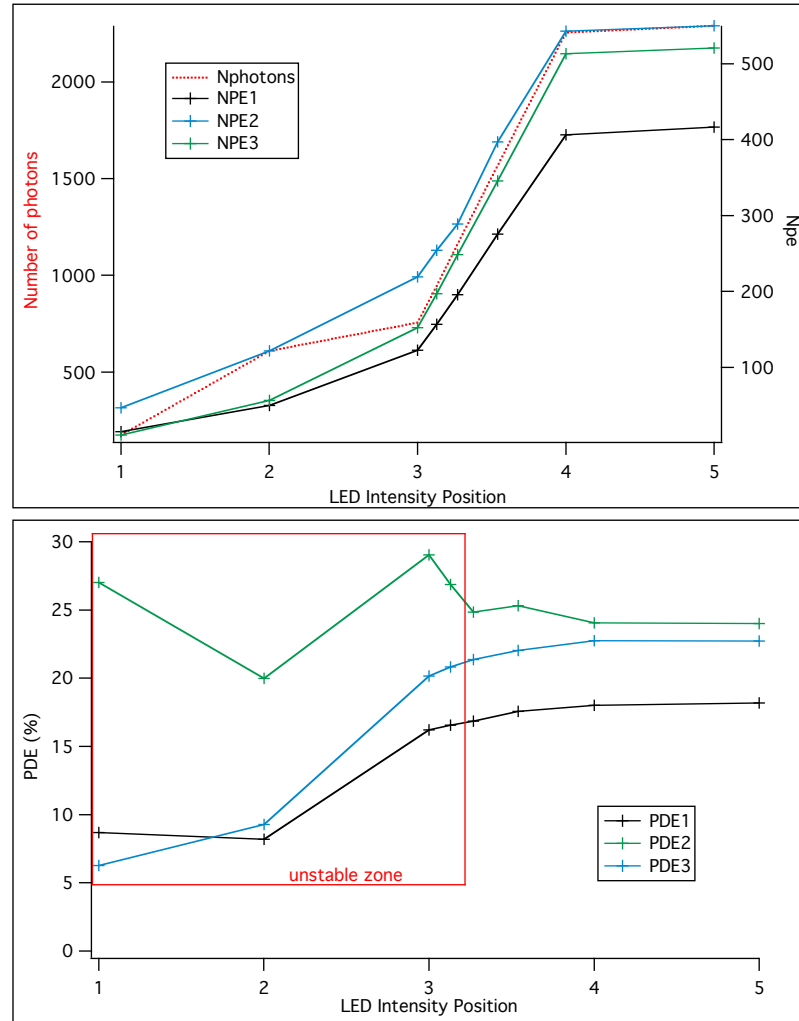


Figure 6.29: Top panel: The number of photons and number of photoelectrons from all three methods are plotted on the left and right vertical axes. Bottom panel: The PDE extracted by all three methods. (original in color)

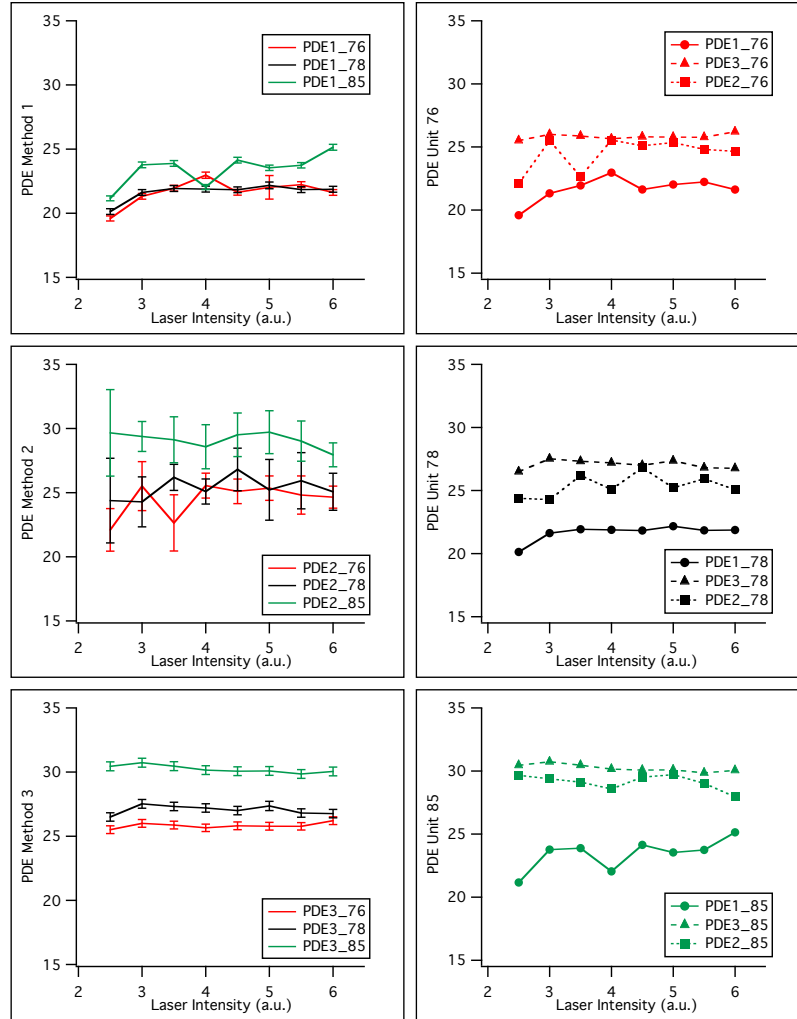


Figure 6.30: PDE values using the laser intensity scan, corrected for the inactive area. (original in color)

Chapter 7

Conclusions

Large-area SiPMs, as the readout for the GlueX experiment, have been tested at the University of Regina. In order to study these SiPMs, gain uniformity tests and PDE measurements were done, as well as minor tests to find out if the set-ups and measurements were repeatable.

For the gain uniformity tests, programming codes were written to control the x-y scanner's movement in four different ways of forward, backward, and random scanning of the cells, as well as cell mapping, in which each cell was divided into four sub-cells. The 10, 2011 article units and the 2010 unit are uniform within the cells, mostly within 10%.

Moreover, for the PDE test, a device was designed, constructed, and tested in order to provide the best possible arrangement for the photodetectors and light sources. The PDE extraction device was additionally tested to assure it provides a symmetric environment, and to assure that the number of photons reaching each end was the

same, and the results from both side of the PDE device were the same within the experimental error. In addition of using three different calculation methods for the PDE extraction, the PDE results were extracted using LED and the laser. The PDE results were more accurate using the laser, and was around $16 - 24\% \pm 2\%$.

The most important advantages of the SiPMs, for the GlueX experiment, compared to conventional PMTs are their relatively small size and immunity to magnetic fields, since there will be a 2.2 T solenoid at the GlueX detector. During the PDE testing, it was also found out that in addition to the dark current and the pedestal contributions, electronic noise was also significant, which was due to the pre-amplifier voltages, since the bias voltage and the light source were off.

For future tests, responses of SiPMs to different temperatures and different magnetic fields should be studied, and additional tests should be carried out on the reliability and signal characteristics of the SiPM electronic boards.

In conclusion, the development and deployment of large-area SiPMs resolved the readout issues for the BCAL, and further developments have promising applications in medical (eg. PET/MRI) and space (sensors, robotics) physics, among other academic and industrial fields.

Bibliography

- [1] M. Poelker. Polarized electron sources and polarimeters 2008. In *PESP*, 2008.
- [2] L.S. Cardman, L. Harwood, and T. Jefferson. The jlab 12 gev energy upgrade of cebafe for qcd and hadronic physics. In *Particle Accelerator Conference, 2007. PAC. IEEE*, pages 58 –62, june 2007.
- [3] JLab 12 GeV Project Team C. H. Rode. Jefferson lab 12 gev cebafe upgrade. In *AIP Conference Proceedings*, volume 1218, pages 26–33. American Institute of Physics, April 9 2010.
- [4] Robert Mann. *An Introduction to Particle Physics And The Standard Model*. CRC Press, 2010.
- [5] B. E. Baaquie A. H. Chan N. P. Chang S. A. Cheong L. C. Kwek C. H. Oh H. Fritzsch, K. K. Phua. *Quantum Mechanics, Elementary Particles, Quantum Cosmology And Complexity, Proceeding of the Conference in Honour of Murray Gell-Mann’s 80th Birthday*. World Scientific Publishing Co.Pte. Ltd., 2011.
- [6] Micah R. Veilleux. The effects of non-flat cathode plane surfaces in drift chambers of the gluex experiment. Master’s thesis, Christopher Newport University, 2010.

- [7] Igor Senderovich. The search for gluonic excitations in light mesons with the gluex experiment. GlueX Talk, GlueX-doc-1957-v1.
- [8] Thanushan Kugathasan. *Lower-Power High Dynamic Range Front-End Electronics for the Hybrid Pixel Detectors of the PANDA MVD*. PhD thesis, University of Turin, 2008.
- [9] Blake D. Leverington. *The GlueX Lead Scintillating Fibre Electromagnetic Calorimeter*. PhD thesis, University of Regina, 2010.
- [10] The GlueX Collaboration. The gluex experiment a search for qcd exotics using a beam of photons. GlueX Note, GlueX-doc-346, October 2004.
- [11] Gergana A. Koleva. Beam tests for the gluex barrel calorimeter prototype. Master’s thesis, University of Regina, 2006.
- [12] The GlueX Collaboration. The science of quark confinement and gluonic excitations, gluex/hall d report. Technical report, 2002.
- [13] Stamatios Katsaganis. The electromagnetic calorimeter of the gluex particle detector. Master’s thesis, University of Regina, March 2011.
- [14] Mitchell Underwood. Design of electronics for a high energy photon tagger for the gluex experiment. Master’s thesis, University of Connecticut, 2010.
- [15] Richard Wigmans. *Calorimetry: Energy Measurement in Particle Physics*. Oxford University Press, November 2003.
- [16] Kuraray Co., LTD., Methacrylate Materials Marketing and Sales Department. *Scintillation Materials*.

- [17] Elton Smith. Update on the bcal readout. GlueX Technical Report, GlueX-doc-1686.
- [18] Erika Garutti. Silicon photomultipliers for high energy physics detectors. *Journal Of Instrumentation*, 6(10):C10003–C10003, 2011.
- [19] Glenn F. Knoll. *Radiation Detection and Measurement*. Don Fowley, fourth edition, 2010.
- [20] Y. Musienko, D. Renker, S. Reucroft, R. Scheuermann, A. Stoykov, and J. Swain. Radiation damage studies of multipixel geiger-mode avalanche photodiodes. *Nuclear Instruments and Methods in Physics Research Section A: Accelerators, Spectrometers, Detectors and Associated Equipment*, 581(12):433 – 437, 2007. VCI 2007, Proceedings of the 11th International Vienna Conference on Instrumentation.
- [21] Patrick Eckert, Hans-Christian Schultz-Coulon, Wei Shen, Rainer Stamen, and Alexander Tadday. Characterisation studies of silicon photomultipliers. *Nuclear Instruments and Methods in Physics Research Section A: Accelerators, Spectrometers, Detectors and Associated Equipment*, 620(23):217 – 226, 2010.
- [22] Fernando J. Barbosa. Summary of the bcal readout tests using sipm arrays. GlueX-doc-1387, December 2009.
- [23] V. Andreev, J. Cvach, M. Danilov, E. Devitsin, V. Dodonov, G. Eigen, E. Garutti, Yu. Gilitzky, M. Groll, R.-D. Heuer, M. Janata, I. Kacel, V. Korbel, V. Kozlov, H. Meyer, V. Morgunov, S. Nmeek, R. Pschl, I. Polk, A. Raspereza, S. Reiche, V. Rusinov, F. Sefkow, P. Smirnov, A. Terkulov, . Valkr, J. Weichert, and J. Zlek. A high-granularity plastic scintillator tile hadronic calorimeter with apd readout for a linear collider detector. *Nuclear Instruments and Methods in*

- Physics Research Section A: Accelerators, Spectrometers, Detectors and Associated Equipment*, 564(1):144 – 154, 2006.
- [24] A. Biland, I. Britvich, E. Lorenz, N. Otte, F. Pauss, D. Renker, S. Ritt, U. Roesner, and M. Scheebeli. First detection of air shower cherenkov light by geigermode-avalanche photodiodes. *Nuclear Instruments and Methods in Physics Research Section A: Accelerators, Spectrometers, Detectors and Associated Equipment*, 595(1):165 – 168, 2008. RICH 2007, Proceedings of the Sixth International Workshop on Ring Imaging Cherenkov Detectors.
- [25] Sascha Moehrs, Alberto Del Guerra, Deborah J Herbert, and Mark A Mandelkern. A detector head design for small-animal pet with silicon photomultipliers (sipm). *Physics in Medicine and Biology*, 51(5):11131127, February 2006.
- [26] Syed Naeem Ahmed. *Physics & Engineering of Radiation Detection*. Academic Press, 2007.
- [27] Kathryn Louise Janzen. Optimization of performance parameters for large area silicon photomultipliers for use in the gluex experiment. Master’s thesis, University of Regina, 2010.
- [28] Web, electrical engineering training series.
- [29] G Bondarenko, P Buzhan, B Dolgoshein, V Golovin, E Guschin, A Ilyin, V Kaplin, A Karakash, R Klanner, V Pokachalov, E Popova, and K Smirnov. Limited geiger-mode microcell silicon photodiode: new results. *Nuclear Instruments and Methods in Physics Research Section A: Accelerators, Spectrometers, Detectors and Associated Equipment*, 442(1-3):187 – 192, 2000.
- [30] P Buzhan, B Dolgoshein, L Filatov, A Ilyin, V Kantzerov, V Kaplin,

- A Karakash, F Kayumov, S Klemin, and E Popova. Silicon photomultiplier and its possible applications. *Nuclear Instruments and Methods in Physics Research Section A: Accelerators, Spectrometers, Detectors and Associated Equipment*, 504(1-3):48–52, 2003.
- [31] Jefferson Lab. Gluex/hall d calorimeter final design and safety review, section 3: Sipm readout for bcal. Technical report, Jefferson Lab, 2008.
- [32] Hamamatsu. *Si APD array S8550-02*.
- [33] *MPPC Multi-Pixel Photon Counter*. Technical Information.
- [34] Roman Greim. Sipm arrays. DPG-Frhjahrstagung, 2009.
- [35] *SensL SPM Technical and Application Notes*, 2007.
- [36] J.E. Moyal. Theory of ionization fluctuations. *Philosophical Magazine Series 7*, 46(374):263–280, 1955.
- [37] GlueX Collaboration. Recent progress on silicon photomultipliers for bcal. GlueX Talk, GlueX-doc-1755, February 2012.

Appendix A

Plots for the Gain Uniformity and the PDE Measurements

For the gain uniformity results different plots were sketched and all of them could not be shown in the main body of the thesis. Thus, this appendix contains more graphs on the gain uniformity tests for the 2010 SiPM unit and the 2011, 10 article units.

A.1 The 2010 SiPM Unit

As mentioned in chapter 5, a study was done for the subcells and their families. Additional result on the study of the those families are shown in figures A.1 and A.2.

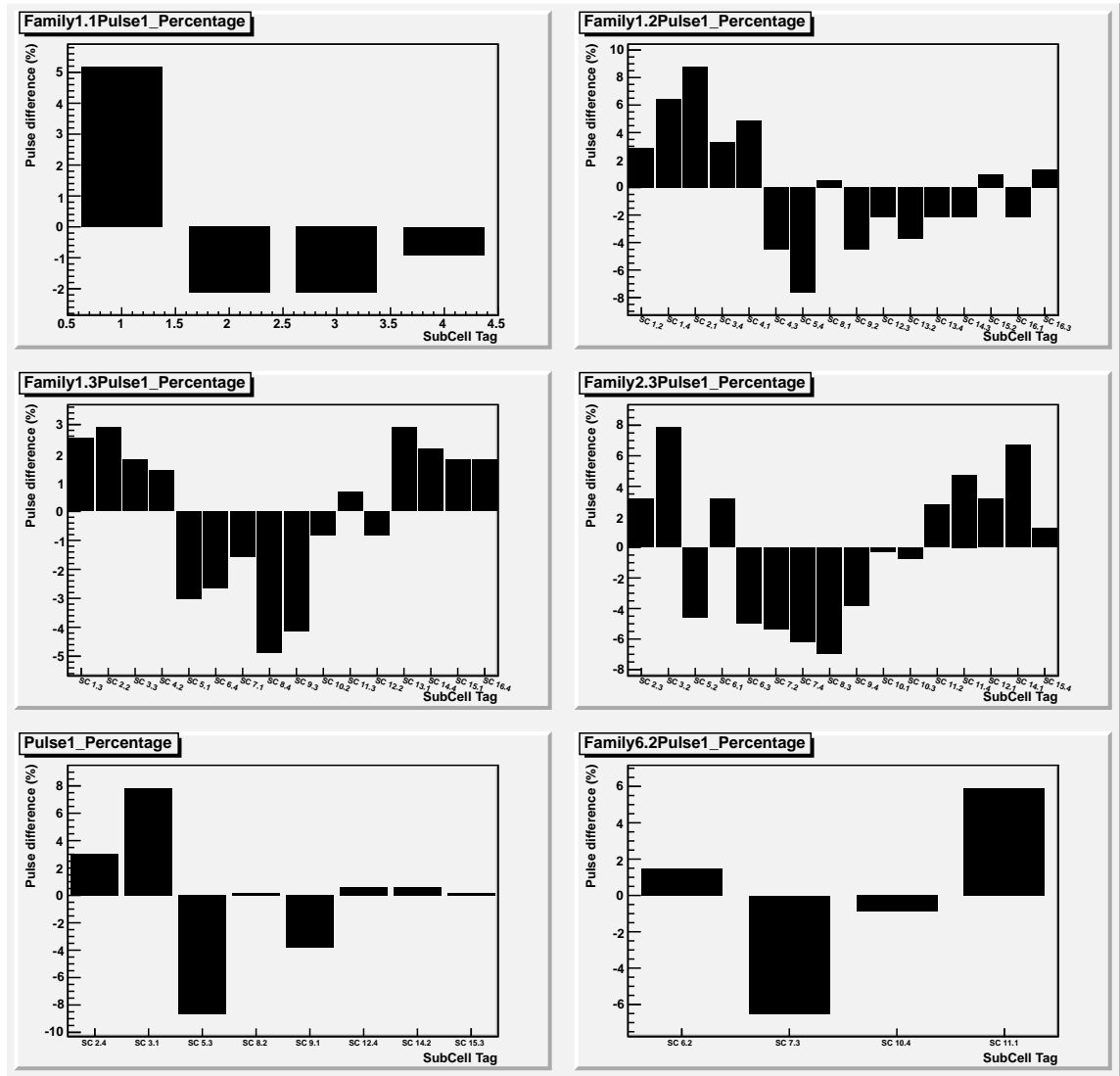


Figure A.1: studying sub-cell families

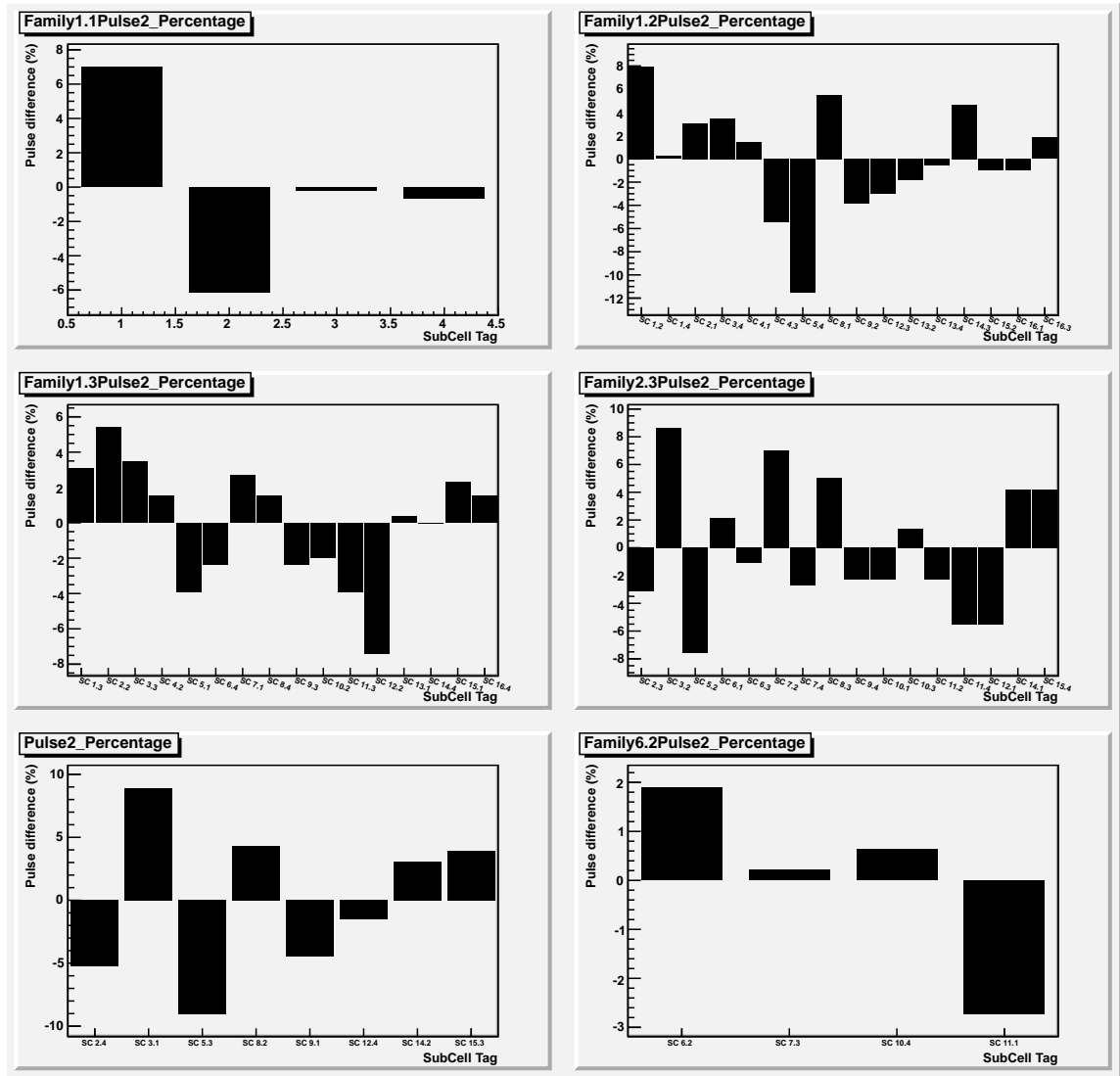


Figure A.2: studying sub-cell families

A.2 The 2011, 10 Article Units

The gain uniformity results for the 10, 2011 article units are shown in figures A.3, A.4, A.5, and A.6. Note that for SiPM units 77 and 81, each of the gain uniformity tests, excluding the cell-mapping, were done five more times to increase the statistics

for those units, since the results of their forward, backward, and random scans were not consistent with each other for the first time that the tests were done.

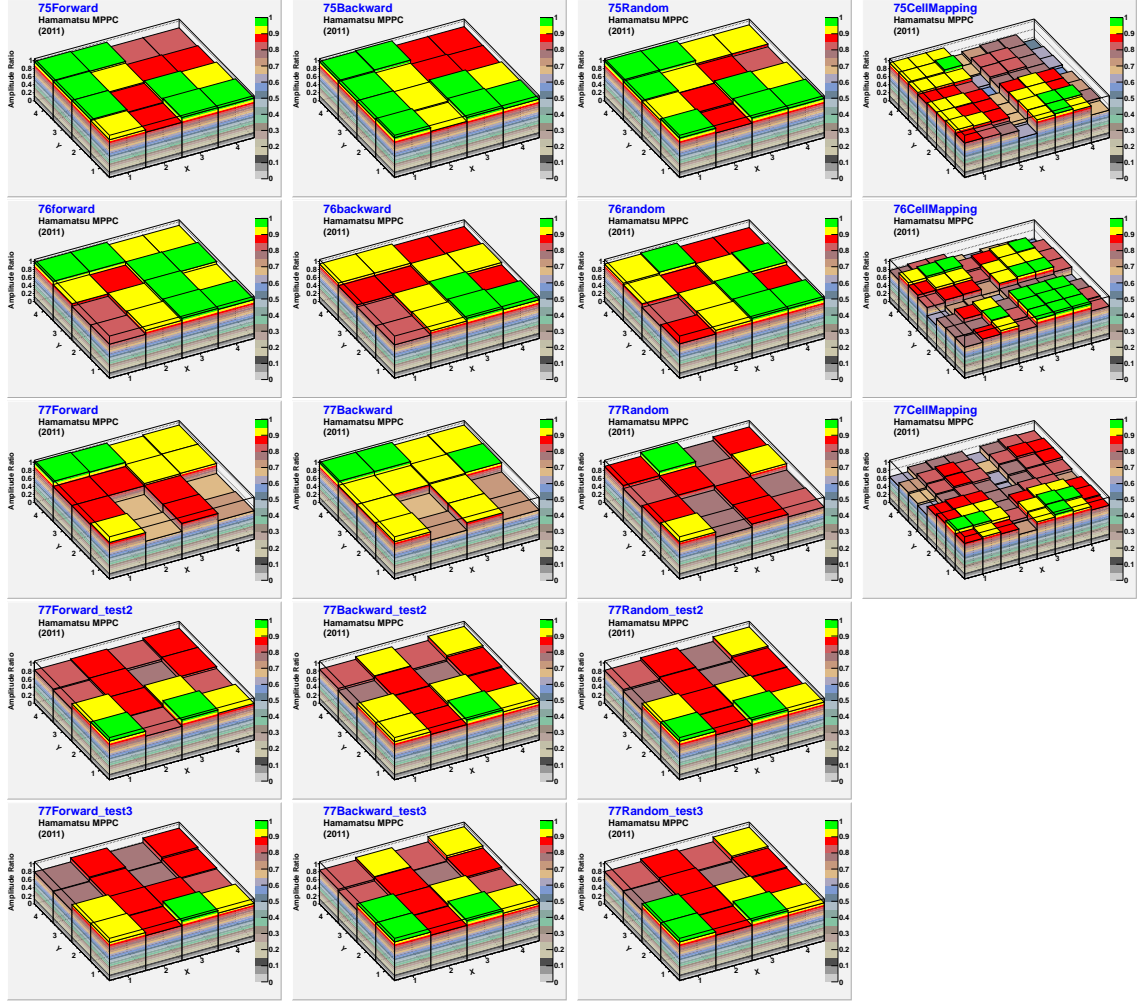


Figure A.3: The first to third rows are the gain uniformity test results for SiPMs #75 to 77, respectively. The forth and fifth rows are the repeated tests for the unit #77, to increase the statistics. The first to forth columns, from left to right, are the forward, backward, random, and cell mapping scans, respectively. (original in color)

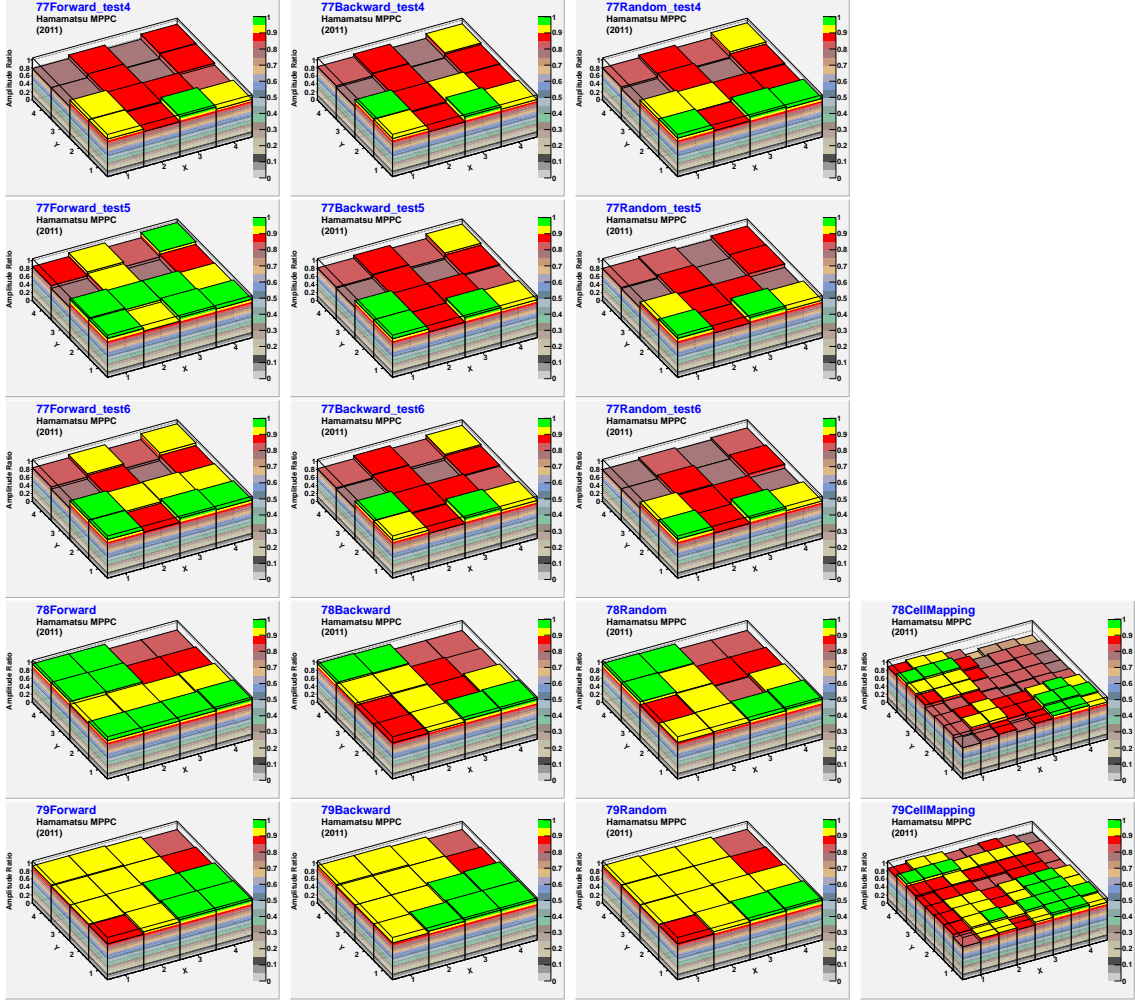


Figure A.4: The first to third rows are the gain uniformity repeated test results for SiPMs #77, to increase the statistics. The forth and fifth rows are the repeated tests for the units #78 and 79, respectively. The first to forth columns, from left to right, are the forward, backward, random, and cell mapping scans, respectively. (original in color)

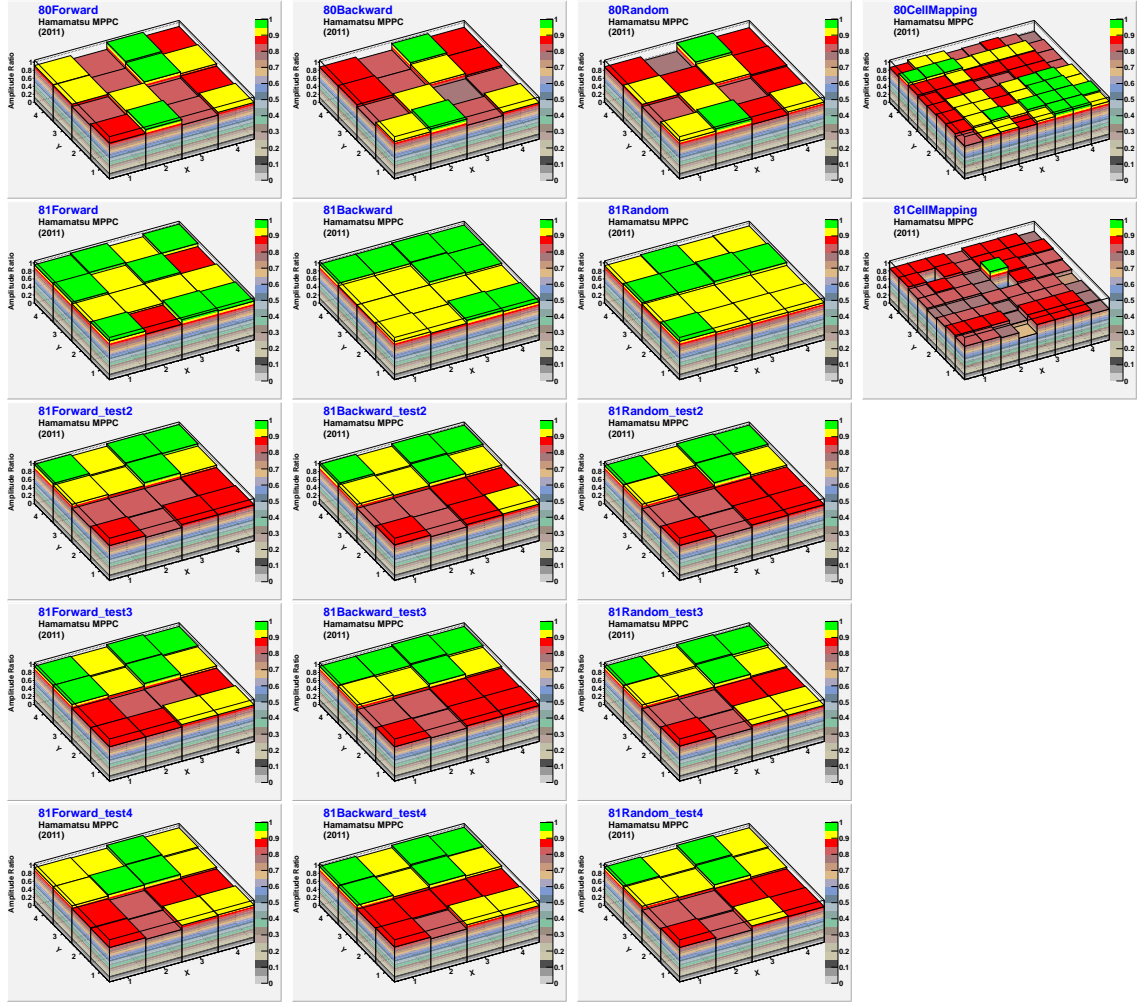


Figure A.5: The first and second rows are the gain uniformity test results for SiPMs #80 and 81, respectively. The third to fifth rows are the repeated tests for the unit #81, to increase the statistics. The first to fourth columns, from left to right, are the forward, backward, random, and cell mapping scans, respectively. (original in color)

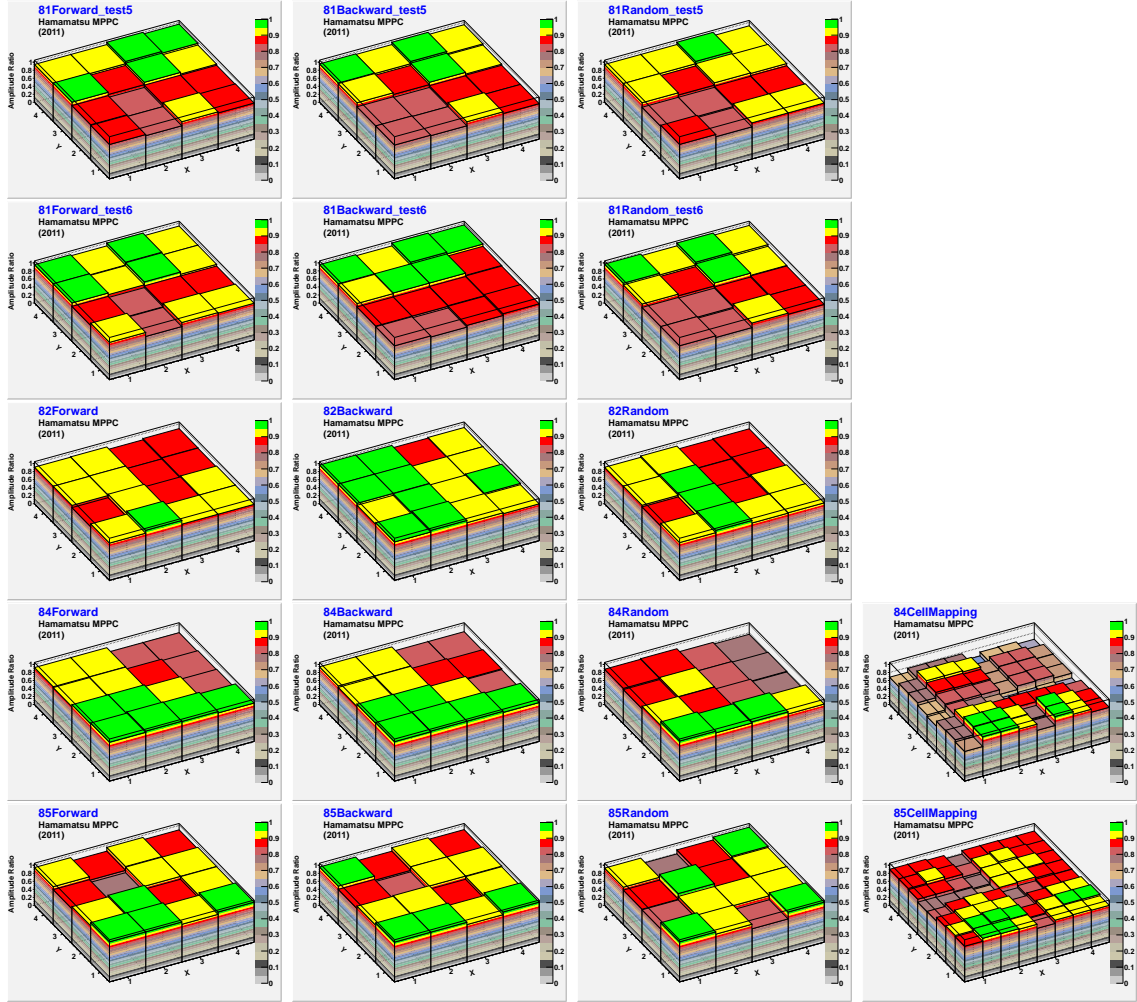


Figure A.6: The first and second rows are the gain uniformity repeated test results for SiPMs #81, to increase the statistics. The third to fifth rows are the repeated tests for the units #82 to 85, respectively. The first to forth columns, from left to right, are the forward, backward, random, and cell mapping scans, respectively. (original in color)